

Iragi National Journal of Earth Science



www.earth.mosuljournals.com

Reconnaissance Geochemical Exploration for Copper Mineralization at Wadi Dara, North Eastern Desert, Egypt

Attia Rabie 1* , M. A. Wahab Gaber 2 , Taher M. Shahin 3 , Ashraf Emam 4 , Mahmoud M. Hassaan 5

Article information

Received: 21- Sep -2024

Revised: 19-Oct-2024

Accepted: 11-Nov-2024

Available online: 01- Oct -2025

Keywords:

Dara

Geochemical Exploration

Cu Ore deposits
Remote sensing

Correspondence: Name: Attia Rabie

Email: attia.rabie@azhar.edu.eg

ABSTRACT

The Wadi Dara area is located in the North Eastern Desert of Egypt. The exposed rock units are metavolcanics, gabbro-diorite, granodiorite, Dokhan volcanics, monzogranite, and alkali feldspar granite. The area is known for bearing Cu-Au mineralization. The samples are collected via fieldwork and studied using remote sensing, microscopic, and geochemical studies to identify the rock types and the center of mineralization with its economic importance. The remotely sensed data identified the main trends of lineaments, which are NE-SW and NW-SE. The recorded alteration types are argillaceous, phyllic, and propylitic types chiefly within granodiorite and gabbro-diorite. The ore minerals are mainly sulfides, chalcopyrite, galena, and sphalerite with supergene minerals. Petrochemically, the rocks exhibit metaluminous, ferroan, alkalic-calcic, while gabbro diorite is tholeiitic. The rocks were formed in syn-collisional to late orogenic fields, and the gabbro-diorite plots formed in an ocean island setting. The geochemical patterns and factors distinguished two fields of ore elements, pointing to the presence of these metals in more than one phase, e.g., sulfides, oxides, and silicates. Geochemically, Au and Cu are the main ore elements in gabbro-diorite with Pb and Mo as the main associated elements. While in granodiorite, the Au is the main ore element, and the Cu is the chief associated element in addition to (As, Pb, Co, and Mo). The detected sequence of zoning points to Au is increasing with depth compared to Cu at a higher level. In consequence, gabbro-diorite and granodiorite are promising for detailed studies using drilling. The associated elements (Pb, Mo, As and Co) are pathfinders in other granitic rocks in the stretch.

DOI: 10.33899/earth.2025.153125.1344, ©Authors, 2025, College of Science, University of Mosul. This is an open-access article under the CC BY 4.0 license (http://creativecommons.org/licenses/by/4.0/).

^{1,3,5} Department of Geology, College of Science, University of Al-Azhar, Cairo City, Egypt.

² Exploration Department, Egyptian Petroleum Research Institute, Cairo, Egypt.

⁴ Department of Geology, College of Science, University of Aswan, Aswan City, Egypt.

الاستكشاف الجيوكيميائي الاستطلاعي لتمعدن النحاس بمنطقة وادي دارا، شمال الصحراء الشرقية، مصر .

 $\stackrel{\circ}{\mathbb{D}}$ عطیه ربیع $\stackrel{\circ}{\mathbb{D}}$ ، محمد عبدالوهاب جابر $\stackrel{\circ}{\mathbb{D}}$ ، طاهر شاهین $\stackrel{\circ}{\mathbb{D}}$ ، أشرف امام $\stackrel{\circ}{\mathbb{D}}$ ، محمد عبدالوهاب جابر $\stackrel{\circ}{\mathbb{D}}$ ، طاهر شاهین $\stackrel{\circ}{\mathbb{D}}$

5,311 قسم علوم الأرض، كلية العلوم، جامعة الأزهر ، القاهرة، مصر .

2 قسم الاستكشاف، معهد بحوث البترول، القاهرة، مصر.

4 قسم علوم الأرض، كلية العلوم، جامعة أسوان، أسوان، مصر.

معلومات الارشفة

تاريخ الاستلام: 21- سبتمبر -2024

تاريخ المراجعة: 19- اكتوبر -2024

تاريخ القبول: 11- نوفمبر -2024

تاريخ النشر الالكتروني: 01- اكتوبر -2025

الكلمات المفتاحية:

منطقة دارا

رواسب خامات النحاس

الاستشعار عن بعد

الاستكشاف الجيوكيميائي

المراسلة:

الاسم: عطيه ربيع

Email: attia.rabie@azhar.edu.eg

تقع منطقة وادي دارا في شمال الصحراء الشرقية بمصر . الوحدات الصخرية المكشوفة هي البراكين المتحولة، والغابرو ديوربت، والجرانوديورايت، وبراكين الدخان، والمونز وجرانايت، وجرانيت الفلسبار القلوي. تشتهر المنطقة باحتوائها على تمعدن النحاس والذهب. وتمت دراسة العينات المجمعة باستخدام الدراسات الحقلية والاستشعار عن بعد والدراسات المجهربة والجيوكيميائية للتعرف على أنواع الصخور ومركز التمعدن وأهميته الاقتصادية. حددت بيانات الاستشعار عن بعد الاتجاهات الرئيسة للتراكيب الجيولوجية وهي شمال شرق-جنوب غرب وشمال غرب-جنوب شرق. وتم تسجيل أنواع التغاير وهي طينية وفيلية وبروبيليتية وتوجد بشكل رئيس داخل الجرانوديوريت والجابرو-ديوريت. وتم تسجيل الكالكوبايرايت، البيريت، الجالينا والسفاليريت مع معادن لاحقة. من الناحية البتروكيميائية، تظهر الصخور بأنها ميتالومينية، قلوبة-كلسية، بينما يتميز الجابرو ديوربت بأنه غنى بالحديد. حيث تكونت هذه الصخور في بيئات متزامنة التصادم إلى بيئات متأخرة التكوبن، وتشكلت الجابرو-ديوريت في بيئة جزر المحيط. ميزت الأنماط والعوامل الجيوكيميائية حقلين من عناصر الخام تشير إلى وجود هذه المعادن في أكثر من طور واحد على سبيل المثال الكبربتيدات والأكاسيد والسيليكات. من الناحية الجيوكيميائية يعتبر Au و Cuهما العنصران الخام الرئيسيان في الجابرو-ديوربت، بينما Mo ، Pbاتمثل العناصر الرئيسة المصاحبة وفي الجرانوديوربت يمثل Au/العنصر الخام الرئيسي، والنحاس هو العنصر الرئيس المرتبط فضلا عن العناصر المرتبطة الأخرى وهي Co, As. ، Pb، As تحديد التتابع الخاص بالخامات حيث يوجد الذهب بالأسفل ويزيد بالعمق مقارنة بالنحاس الذي يوجد على السطح. ونتيجة لذلك، يعد الجابرو- ديوريت والجرانوديوريت واعدين لإجراء دراسات تفصيلية باستخدام الحفر. وتعتبر العناصر المرشدة هي

DOI: 10.33899/earth.2025.153125.1344, © Authors, 2025, College of Science, University of Mosul. This is an open-access article under the CC BY 4.0 license (http://creativecommons.org/licenses/by/4.0/).

الرصاص والموليبدينوم والزرنيخ والكوبالت في الصخور الجرانيتية الأخرى في المنطقة.

Introduction

The Eastern Desert (ED) of Egypt represents the western section of the Arabian Nubian Shield (ANS) that is classified into three domains: southern (SD), central (CD), and northern (ND) domains (Stern and Hedge, 1985). Four tectonic stages have been identified for the crustal evolution of ANS, starting some 950 Ma ago (Gass and Ed, 1982; Bentor, 1985; Stern et al., 1988; Stern and Kröner, 1993). The rifting is followed by seafloor spreading and subduction-related formation of oceanic crust and island arc terranes during the early two stages (first stage of 950–850 Ma, and second stage of 850–650 Ma). At the end of the second stage, welding and accretion of oceanic and island arc terranes were the predominant processes. Throughout the third stage (650–580 Ma), the post-collision, large-scale calc-alkaline, intermediate to felsic batholiths were generated. The post-orogenic fourth stage (600–530 Ma) included the formation of intracratonic within-plate alkaline to peralkaline granites. The Northeastern Desert (NED) is

abundant in metamorphic volcano-sedimentary rocks that are Dokhan Volcanics (DVs) and Hammamat sediments (HS) in addition to granitoid complexes (Willis et al., 1988).

Wadi Dara area (W. Dara), located in the NED, encompasses the largest outcrops of granitoid rocks represented by metavolcanics, diorite, muscovite trondhjemite, granodiorites, monzogranites, and alkali feldspar (A F) granite that are cross-cut by abundant dykes. The granitoid rocks have intruded the metavolcanics, the oldest rocks in the area. The DVs occur in the study area either as successions of volcanic rocks or as thick volcano-sedimentary sequences, whereas the HS comprise successions of conglomerate, sandstone, siltstone, mudstone, and turbidities (Eliwa et al., 2014). The area is located between the latitudes 28° 00'and 27° 54'N and longitudes 32° 50'and 33° 02'E (Fig. 1); it is a type locality of copper mineralization in the ED of Egypt. The copper mineralization occurs in six quartz veins hosted in the diorite and granodiorite (Helba et al., 2021). In addition to dacite (Bishady et al., 2001). Hassaan and Al-Hawary (1989) recorded copper sulfide mineralization in 21 lenses, load shape, and irregular veins.

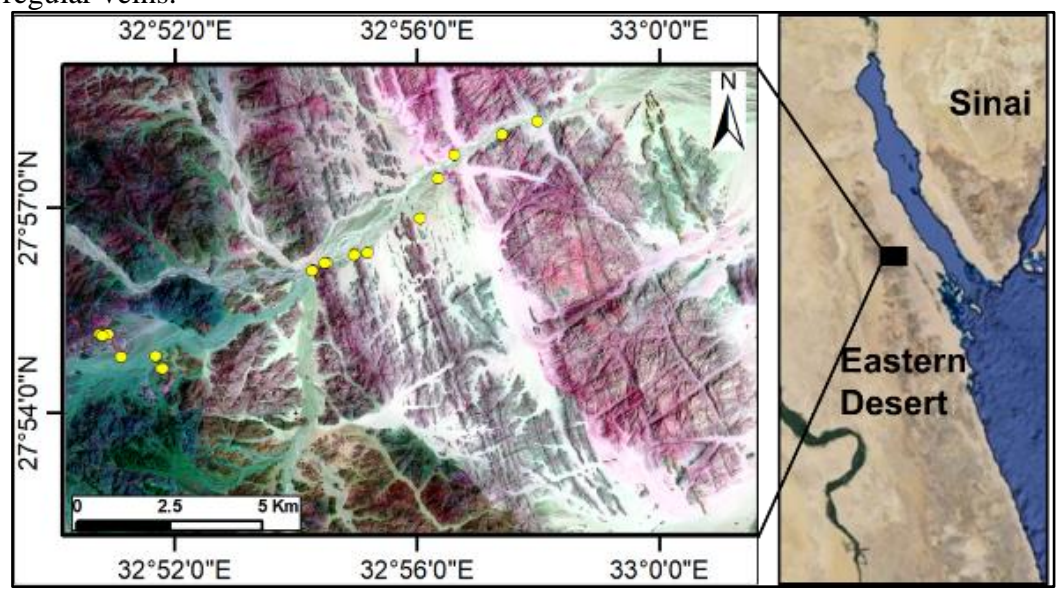


Fig. 1. Location map of the study area with sample sites (Sentinel 2 bands 12-2-8).

Generally, copper mineralization has been identified in various types of metallogenic ore systems, which include magmatic sulfides containing copper, nickel, cobalt, and iron (Cu-Ni-Co-Fe), porphyry copper deposits associated with molybdenum and gold (Cu-Mo-Au), lowsulfur iron oxide-copper-gold (IOCG) deposits, as well as secondary copper deposits enriched through supergene processes and oxide minerals (Pohl, 2011). In the ED of Egypt, many types of Cu mineralization have been identified in the southern and northern domains. The SED includes Cu-Pb-Zn sulphide deposits hosted in meta-rhyodacite volcanics (Atshan, Derhib, and Um Smiuki mines) and Hamash Cu porphyritic granodiorite. Moreover, at the NED, Um El Balad-Dara, Cu-Mo mineralization is recorded in affiliation with Au, chiefly at Um El Balad.

The porphyry copper deposits (PCD) have been formed from high-temperature magmatic hydrothermal fluids (Piragno, 2009). These deposits are characterized by sulfide and oxide ore minerals that formed in veinlets and disseminations in large volumes of hydrothermally altered rocks. They are related to hypabyssal porphyritic dioritic to granitic intrusions with aplitic groundmass (Seedorff et al., 2005). Copper, molybdenum, and gold are the most important commodities of the PCD, in which Cu (> 65% production) and Mo (> 95% production) with significant Au production (Ridley, 2013).

The source of mineralization at W. Dara is stratigraphic and tectonic, based on the absence of any sign of hydrothermal alteration aureole around the ore bodies and quartz veins. The genetic mechanism is the concentration of sulfides along fractures by magmatic process, followed by metamorphism (Hassaan and Al-Hawary, 1989). The magmatic process may be the source of Cu mineralization as a litho-tectonically controlled deposit; in addition to the hydrothermal solutions and or meteoric water, are causes different types of hydrothermal alterations in granodiorite (Bishady et al., 2001). Based on the results of hydrothermal alteration studies, the genesis of Cu mineralization may be PCD type (Al-Boghdady et al., 2003). Helba et al. (2021) defined two stages of hydrothermal solutions, which are both characterized by high H⁺ and K⁺ activity. The IOCG is suggested as a source of mineralization.

Different types of hydrothermal alterations characterize the PCD: potassic, phyllic, sodic calcic, sericite, argillic, and propylitic alterations. These alterations contain mineral assemblages with diagnostic spectral absorption features in the visible - near infrared (VNIR) and shortwave infrared (SWIR) (0.4– $2.5~\mu m$) and/or the thermal infrared (TIR) (8.0–14.0 μm) wavelength regions (Abrams et al., 1983; Abrams and Brown, 1984; Spatz et al., 1995). The mineral assemblages can be discriminated from one another by using their spectral absorption features, which are detectable by multispectral and hyperspectral satellite data. The Advanced Spaceborne Thermal Emission and Reflection Radiometer (ASTER) remote sensor includes high spectral resolution in the SWIR bands for mapping hydrothermal alteration mineral zones (Pieri and Abrams, 2004). The ASTER-SWIR data can be supportive for identifying the alteration mineral assemblages such as: (i) alunite and pyrophyllite; (ii) kaolinite, mica, and cholorite groups; and (iii) epidote, calcite, and dolomite (Huntington, 1996). In addition to mapping of alteration zones, the ASTER data are the most useful for mapping the rock units and mineral targets, especially for Fe oxides.

The objective of the present study is to use the integrated remote sensing, fieldwork, petrographic, and geochemical data for lithological mapping and delineation of hydrothermal alteration zones in the W. Dara area. Remote sensing techniques will be applied for ASTER and Sentinel-2 data, combined with field verification and petrographic description. In addition, the geochemical characteristics of the studied rock units will be investigated, especially the trace element characteristics, to locate and understand the Cu-Au mineralization in the area.

Geologic Setting

The chronological sequence of the surveyed Neoproterozoic basement rocks of the Wadi Dara area is essentially built of island arc-related rocks (metavolcanics and gabbro-diorite rocks), syn-, late-, and post-collision rock units (granodiorite, DVs, HS, monzogranite and AF granites (Fig. 2). These rocks are cut across by a series of dykes and veins.

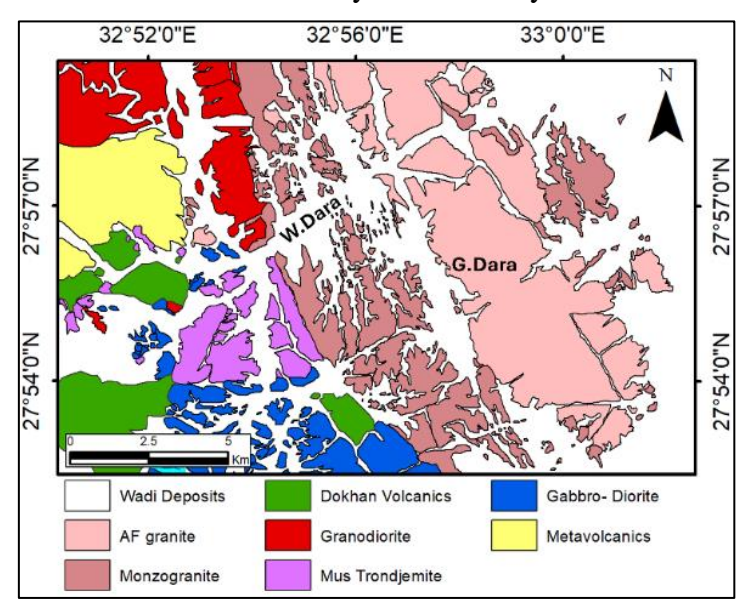


Fig.2. Geologic map of the study area (modified and compiled after Breitkreuz et al., 2010; Jakob et al., 2015).

The gabbro-diorite occurred as isolated small low relief outcrops (Fig. 3a). This rock unit is coarse-grained with dark green and black colors, malachite staining, quartz veins, and sheared diorite (Fig. 3b and c). The granodiorite exposures are jointed, intersected by faults, and quartz veins. This rock is stained by malachite and iron oxides due to alteration of copper and iron mineralization, where the old mine workings are obvious in the field (Figs. 3d-f). Dokhan Volcanics (DVs) occupied Gabal El Kharaza to the northwest of W. Dara as successions of volcanic rock units or as thick volcano-sedimentary successions. They form high outcrops (Fig. 3a).

The monzogranite intrusions vary in size, ranging from small to massive, and have NW-SE directions, running parallel to Gabal Dara, which is situated to the west of the former. Dyke swarms with different compositions intersect these granitic intrusions. The monzogranite intrusions exhibit gentle slopes, exfoliation characteristics and their outcrops possess an onion-like shape (Fig. 3g). In some sites, basic and felsite dykes, as well as AF granitic dykes cut across the monzogranite intrusions (Fig. 3h). The AF granite is the latter pulse of the granitic magma in the area and covers mostly the eastern section of the area. It occurred as moderate to high reliefs, intrudes directly into the monzogranite at Gabal Dara (Fig. 3 h), which is traversed by abundant NE and NW dykes (Fig. 3i) and faults, as well as E-W strike—slip faults.

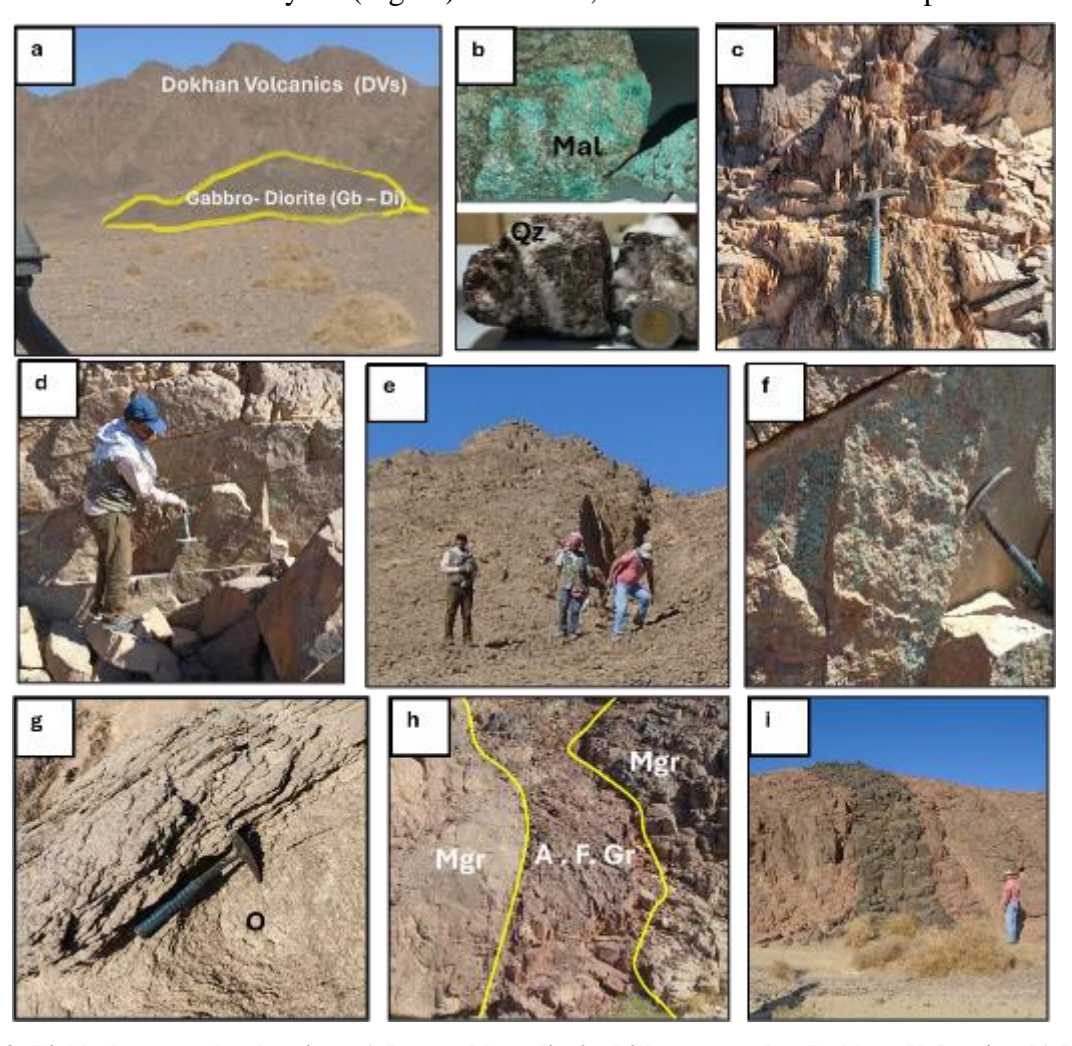


Fig.3: Field photographs showing: a) Low gabbro-diorite hill compared to Dokhan Volcanics; b) Hand specimen sample of stained malachite and quartz veinlets in gabbro-diorite; c) Sheared diorite; d) Two fracture systems in granodiorite; e) Old mining mine work; f) Malachite staining in granodiorite; g) Onion-like shape of monzogranite; h) Contact between monzogranite (Mgr) and AF granite; i) Mafic dyke cutting AF granite.

The monzogranite intrusions vary in size, ranging from small to massive, and have NW-SE directions, running parallel to Gabal Dara, which is situated to the west of the former. These

granitic intrusions are intersected by dyke swarms with different compositions. The monzogranite intrusions exhibit gentle slopes, exfoliation characteristics and their outcrops possess an onion-like shape (Fig. 3g). In some sites, basic and felsite dykes, as well as AF granitic dykes cut across the monzogranite intrusions (Fig.3h). The AF granite is the latter pulse of the granitic magma in the area and covers mostly the eastern section of the area. It occurred as moderate to high reliefs, intrudes directly into the monzogranite at Gabal Dara (Fig.3 h), which is traversed by abundant NE and NW dykes (Fig.3i) and faults, as well as E-W strike—slip faults.

Materials and Methods

During the field work, sampling and structural measurements were carried out, where 25 representative samples were collected. Thirteen samples were prepared for making thin sections and polished surfaces to study the mineral constituents and ore minerals using polarizing and ore microscopes. Moreover, to analyze major and trace elements, fifteen samples were crushed and well pulverized using the normal sequence of fractionation. The analyses were performed using an X-Ray Fluorescence (XRF) spectrometer (Supermini 200 model, manufactured by Rigaku, Japan). This XRF spectrometer operates under vacuum/helium conditions and is equipped with a 200 W x-ray tube. The analyses were conducted at the Egyptian Petroleum Research Institute (EPRI), Cairo, Egypt. The Au was analyzed using the atomic adsorption technique at the Egyptian Mineralogical Resources Authority (EMRA), Cairo, Egypt.

During the field work, sampling and structural measurements were carried out, where 25 representative samples were collected. Thirteen samples were prepared for making thin sections and polished surfaces to study the mineral constituents and ore minerals using polarizing and ore microscopes. Moreover, in order to analyze major and trace elements, fifteen samples were crushed and well pulverized using the normal sequence of the fractionation. The analyses were performed using an X-Ray Fluorescence (XRF) spectrometer (Supermini 200 model, manufactured by Rigaku, Japan). This XRF spectrometer operates under vacuum/helium conditions and is equipped with a 200 W x-ray tube. The analyses were conducted at the Egyptian Petroleum Research Institute (EPRI), Cairo, Egypt. The Au was analyzed using the atomic adsorption technique at the Egyptian Mineralogical Resources Authority (EMRA), Cairo, Egypt.

The present study used remote sensing data of ASTER (Granule ID: AST L1T 00303182003083631_20150427165322_41488, acquired on 18 March 2003) and Sentinel 2B MSI (Granule ID: S2B MSIL1C 20220719T081609_N0400_R121T36RVR 20220719T 091239 and S2B MSIL1C 20220719T081609_N0400_R121_T36RWR_20220719T091239, acquired on 19 July 2022). The data have been processed using the ENVI 5.1 software and Sentinel Application Platform (SNAP) software version 8, in addition to the PCI Geomatica 2018 software for the automated lineaments extraction. Three types of corrections have been done for ASTER data: crosstalk, radiometric, and atmospheric FLAASH corrections using the ENVI 5.1 software. Then, the data processing techniques, including band Ratio (BR), principal component analysis (PCA), were applied for detecting the iron oxides and hydrothermal alteration zones. The band ratio images were processed for highlighting certain features or materials that cannot be seen in the raw bands (Inzana et al., 2003; Pour and Hashim, 2012). Mineralogical Indices using ASTER SWIR bands by Ninomiya (2003) were applied for mapping hydrothermal alteration. These indices are: OH-bearing minerals index OHI = (B7/B6) *(B4/B6), alunite index ALI = (B7/B5) *(B7/B8), kaolinite index KLI = (B4/B5) *(B8/B6), and calcite index CLI = (B6/B8) *(B9/B8). The false color composite (FCC) is an image enhancement technique where the three additive colors of red, green, and blue are used to display multispectral bands, where the minerals show a maximum in their spectral reflectance. The possible color composites (R-G-B) of nine ASTER (SWIR and VNIR) are 84. For highlighting the best combinations of color composite based on information, the optimum index factor (OIF) is used, which is defined as a statistical value that can be used to select the optimum combination of three bands satellite image to produce a color composite (Chavez et al., 1982; Emam et al., 2018; Shebl and Csámer, 2021). To calculate the OIF's highest ranking, the ILWIS software is used.

The Clarke of concentration (CC) which is a factor to distinguish the anomalous from the normal geochemical background samples for each rock unit. The factor is calculated by dividing the content of the elements in samples of the studied rock units by the reference given by Turekian and Wedepohl (1961). The element content is normal when the CC value is between 0.5 and 1.78 (Hassaan et al., 1991; Kviatkovisky, 1977). The element having a CC value < 0.5 or >1.78 is considered to be negative or positive anomalous, respectively. The CC values would also be used to distinguish the geochemical association of mineralization. The zoning coefficient factor is calculated to indicate the zoning sequence of ore elements that form the mineral deposit (Hassaan, 2011). The zoning coefficient (z) measures the change from the center or periphery of the ore body using CC, or productivity Mi of the elements.

Results

Remote Sensing

Remote sensing techniques are applied to the ASTER and Sentinel-2B MSI data to show the spectral aspects of the study area, which are beneficial for mapping of rock units and delineation the mineralization zones.

1. Lineaments Extraction

The structural lineaments representing major faults of the area are manually traced from the processed false FCC images of ASTER bands 731 as RGB and Sentinel-2B bands (R: 12, G: 8, B: 3) (Fig. 4a). Moreover, the automated extraction of lineaments is carried out using the computer software PCI Geomatica version 16 (Fig. 4b). Wadi Dara area is a part of the ANS that was affected by the Red Sea graben systems. There are three main fault systems observed in the NE-SW, NW-SE, and E-W directions.

The faults comprise the dry valleys (Wadis) of the area (Fig. 4a). F1 fault system (blue lines) represents the direction NE-SW represented by W. Dara that cuts G. Dara and extends SW to the investigated rock units. The F2 fault system (red lines) represents the direction NW-SE while the monzogranites occurred in the same direction. Moreover, the line density map is created to highlight the most structure-dense areas that occurred in three areas (north of G. Dara, S. G. Dara related to F1 fault system, and west of G. Dara) (Fig. 4c). The trend analysis using rose diagram (Fig. 4d) shows two main directions, the first is NE while the other is NW; the trends are similar to the manual extracted lineaments.

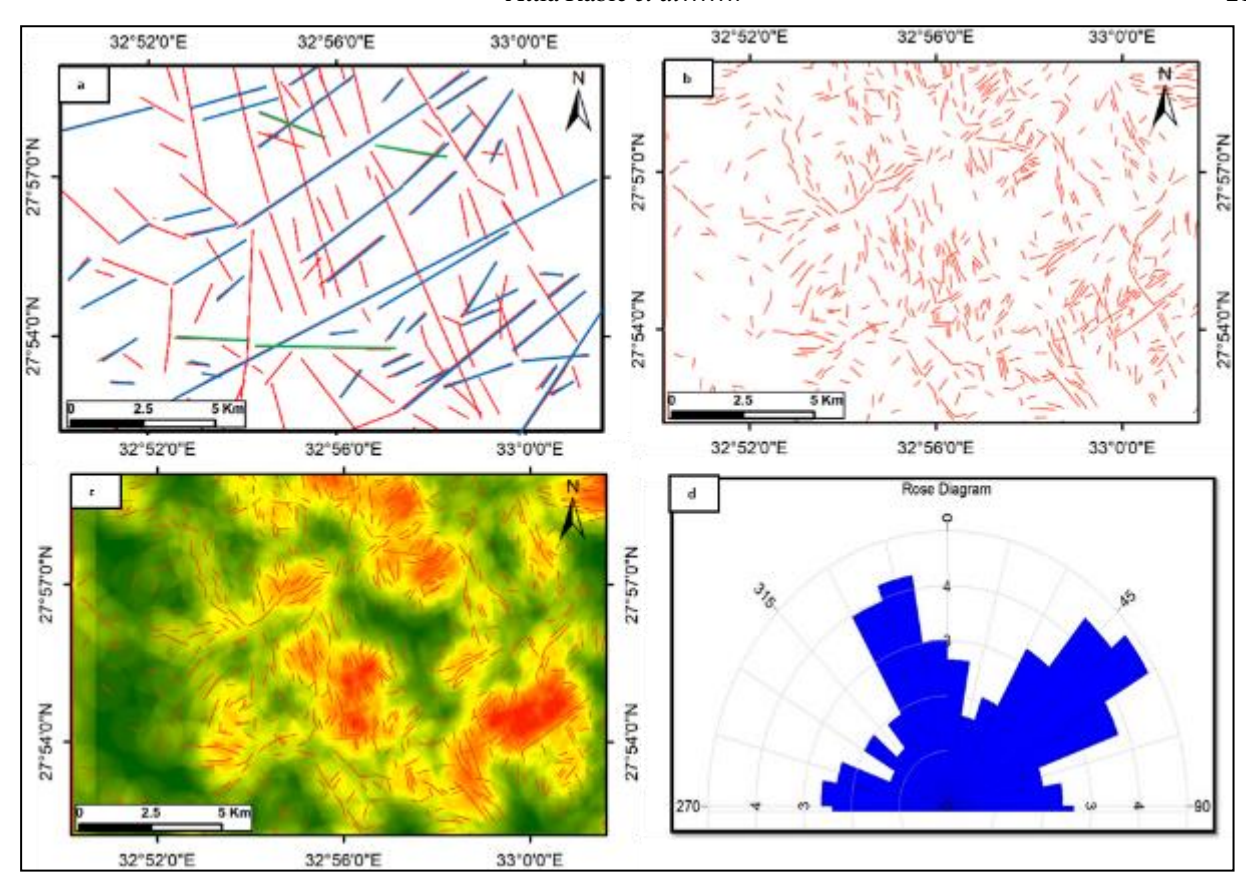


Fig. 4. Photograph showing a) Manual extracted lineaments; b) Automated extracted lineaments; c) Line density map showing the highly structured areas with automated lineaments; d) Rose diagram showing the main trend directions.

2. Lithological Mapping

For the lithological mapping, the ASTER and Sentinel-2B data were processed using OIF, FCC, band ratios, and PCA techniques. The results of the OIF algorithm are applied for the ASTER and Sentinel 2 reflected VNIR-SWIR bands, showing six false color band combinations with the highest OIF values (Table 1). According to the OIF results, the ASTER band combinations (R: 8, G: 6, B: 1) and (R: 9, G: 2, B: 1), as well as the Sentinel-2B band combinations (R: 6, G: 5, B: 1) and (R: 6, G: 3, B: 1) discriminate clearly the different rocks occupying the area. However, the Sentinel 2B band combinations have higher spatial resolution than that of ASTER band combinations, so they are recommended to be used for distinguishing the rock units (Figs. 5a to d).

Table 1: OIF index highest ranking of ASTER and Sentinel 2B (VNIR-SWIR) bands.

		ASTER	band (b)			Sentinel -2 b	ands (b)	
N	R	G	В	Ratio	R	G	В	Ratio
1	b 9	b 8	b 1	77.00	b 12	b 4	b 2	73.91
2	b 9	b 2	b 1	76.4	b 12	b 11	b 2	73.86
3	b 8	b 2	b 1	76.31	b 12	b 8	b 2	73.82
4	b 8	b 7	b 1	76.26	b 12	b 3	b 2	76.66
5	b 8	b 6	b 1	76.22	b 11	b 4	b 2	73.58
6	b 9	b 7	b 1	76.16	b 11	b 8	b 2	73.49

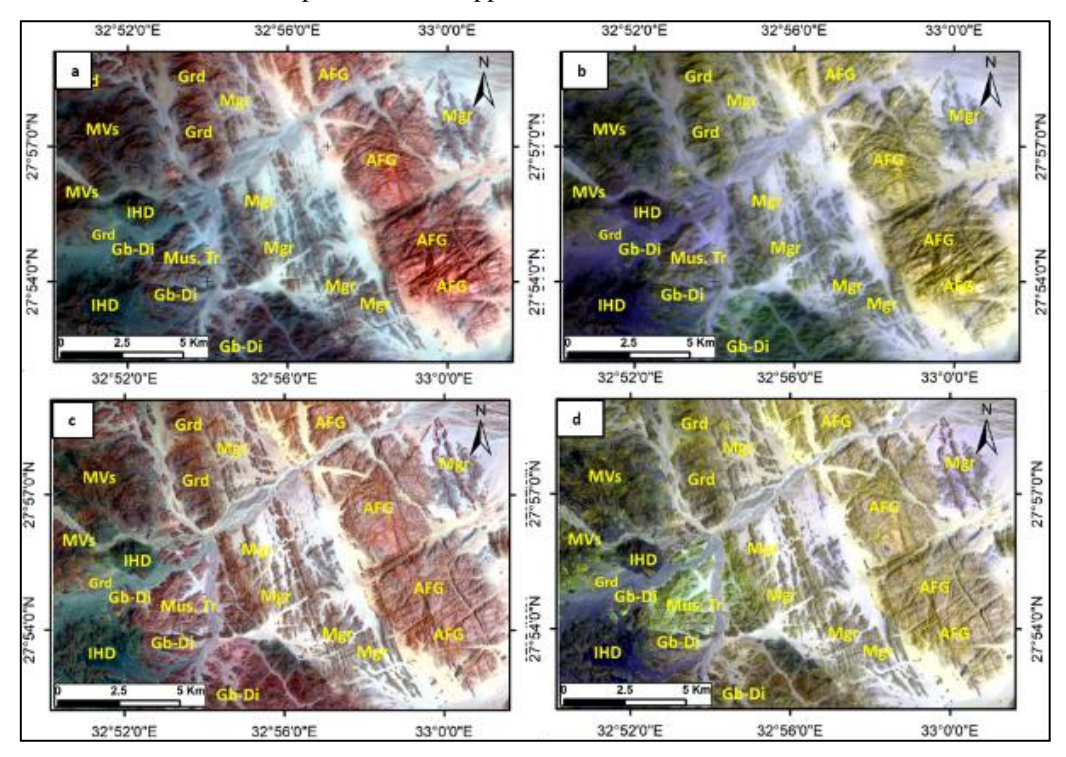


Fig.5. Photograph showing the OIF results of ASTER and Sentinel 2 data. a) ASTER OIF 861; b) ASTER OIF 921; c) Sentinel 2 OIF 12/11/2; d) Sentinel 2 OIF 12/4/2.

The ASTER FCC image (R:4/7, G:3/4, B:2/1) well discriminates the interbedded Hammamat-Dokhan volcanics (IHD) with light green color, while the ASTER FCC image (R: 4/7, G: 4/1, B: 2/3*4/3) distinguishes the Mus trondjemite with white color and the IHD with red color (Figs. 6a and b). The Sentinel 2B FCC image (R:3, G:11, B:12) illustrates all rock units, where the diorite-granodiorite appears with grey color, the Mus trondjemite has light green color, the IHD has dark red color, while the AF granite exhibits sky blue color. Moreover, the ASTER PC image (R: PC1, G: PC2, B: PC3) differentiates clearly the AF granite (purple), IHD (white to pink), and granodiorite (brown). (Fig. 6c and d).

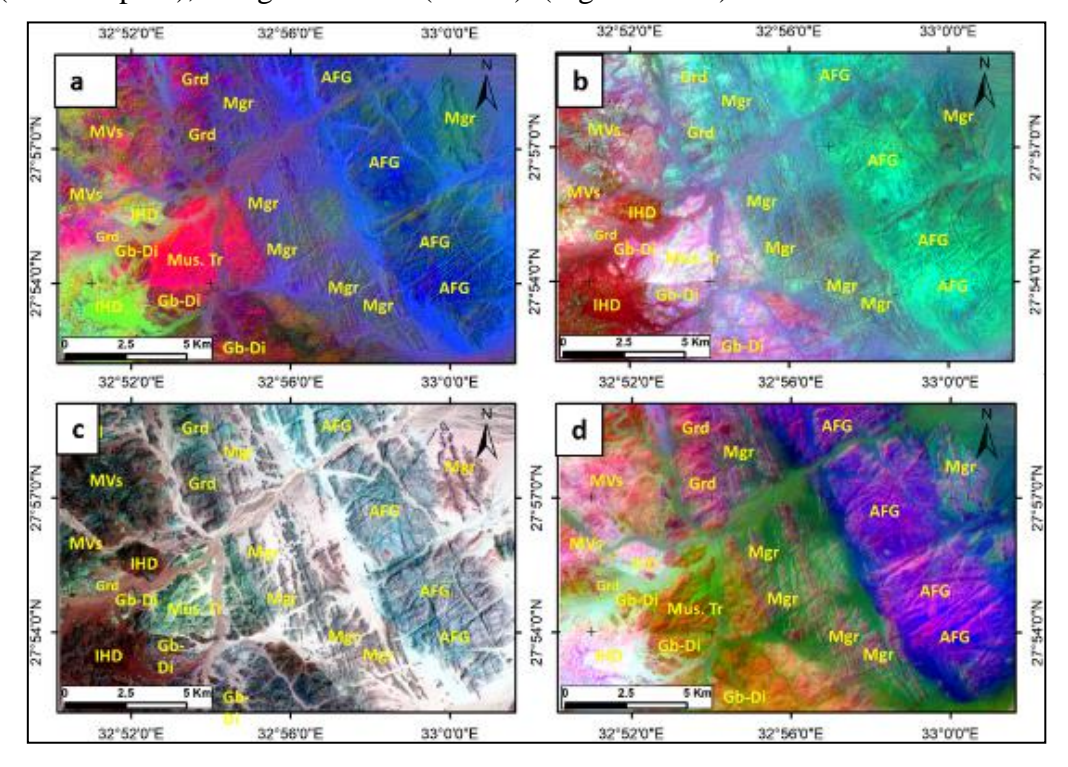


Fig. 6. FCC images of lithological mapping. a) (4/7, 3/4, 2/1) ratio of Abrams et al. (1983); b) (4/7, 4/1, 2/3*4/3) ratio of Sultan et al. (1986); c) Sentinel 2 bands (3/11/2); d) ASTER PCA (1/2/3).

3. Mapping of Hydrothermal Alteration Zones

The hydrothermal alteration zones are useful for locating the mineral deposits. Different deposits occur with specific types of hydrothermal alterations such as argillaceous, phyllic, potassic, sodic, and propylitic. Remote sensing data can be utilized to detect and delineate these types.

The propylitic alteration (450° to 600° C) can be mapped using the ASTER ratio for epidote and chlorite minerals, while the calcite index (CI) is used for mapping calcite (Figs. 7a and b). The Propylitic alteration zones occur in the granodiorite and Mus trondjemite with minor alteration in monzogranite, in the south of the study area. Epidote, chlorite, and calcite are the essential minerals with pyrite in many cases. The Fe oxides, sericite, and apatite are also present (Ridley, 2013). The phyllic alteration can be mapped using the ASTER band ratio (7/6) and the OH index, which are best for discriminating the muscovite and other OH-bearing minerals (Fig. 7c and d). The phyllic alteration (200° to 450° C) is characterized by quartz-sericite-pyrite (QSP), where the fine-grained dioctahedral white micas (muscovite) is known as sericite (Pirajno, 2009).

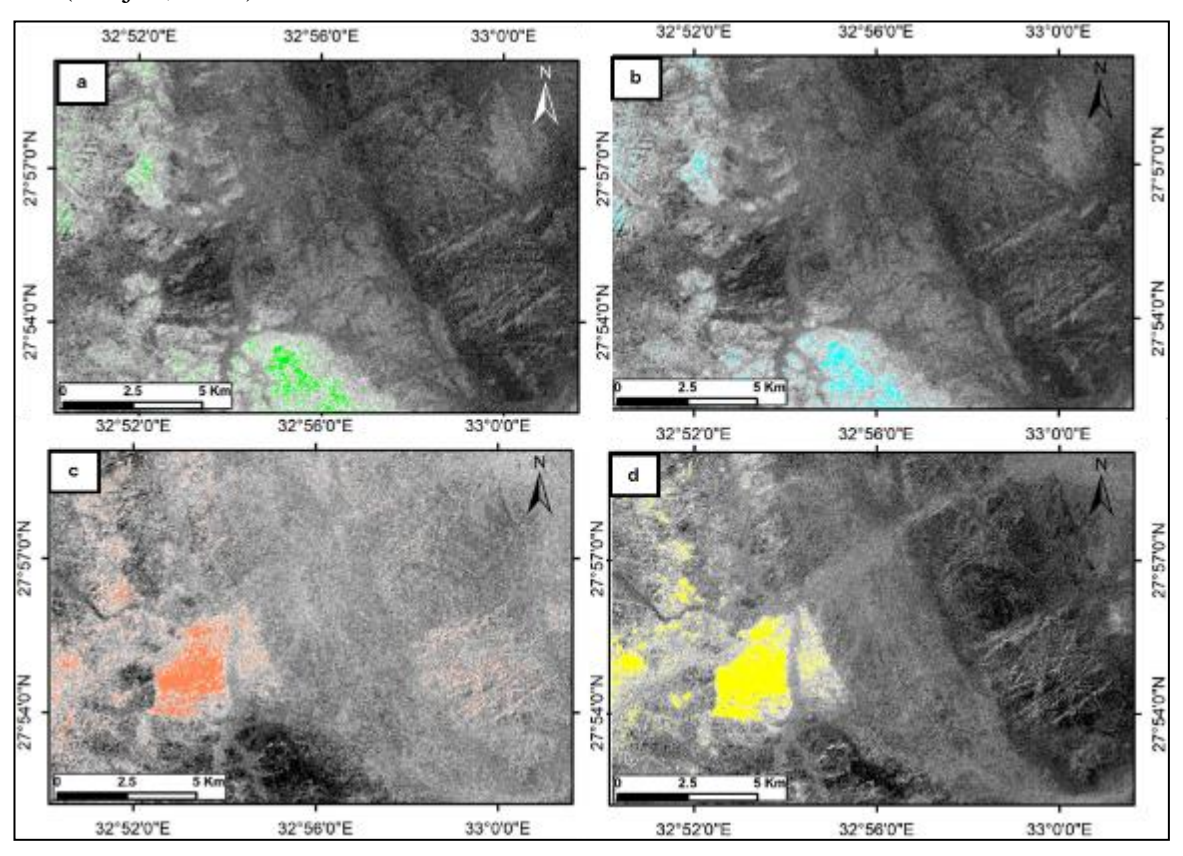


Fig. 7. ASTER images of hydrothermal alteration zones. a) 6+9/8 epidote-chlorite; b) Calcite index. c) 7/6 muscovite; d) OH index.

The argillaceous alteration (100° and 300° C) can be mapped using the ASTER band ratio (4/6) that clearly discriminates the clay minerals. Moreover, the kaolinite index (KI) is used for mapping kaolinite (Figs. 8a and b). The processed ratios indicate that the argillaceous alteration zones are located at the Mus trondhjemite and granodiorite units to the west of the area. In the argillaceous alteration, kaolinite and montmorillonite are the main clay minerals, with subordinate amounts of other minerals like biotite, illite, chlorite, pyrophyllite, diaspore, alunite, sulfides, quartz, and andalusite (Ridley, 2013).

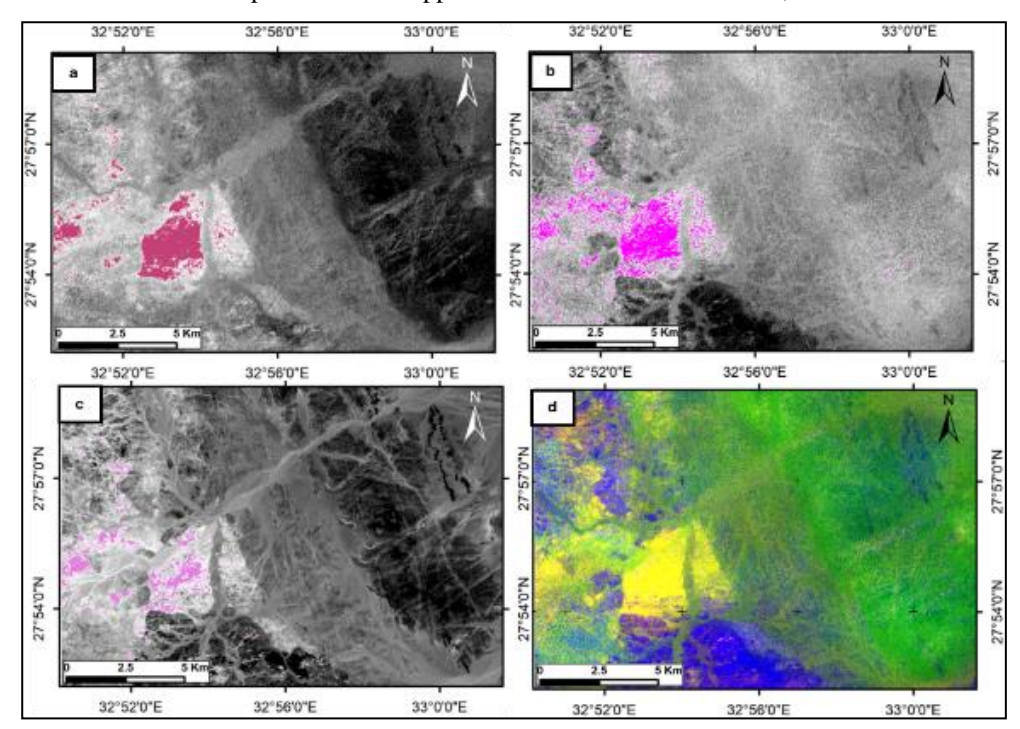


Fig. 8. ASTER images of hydrothermal alteration zones; a) 4/6 clay minerals; b) Kaolinite index; c)11/12 of Sentinel 2B Alteration zones; d) RGB (OH/Kl/Cl) image of the combined indices.

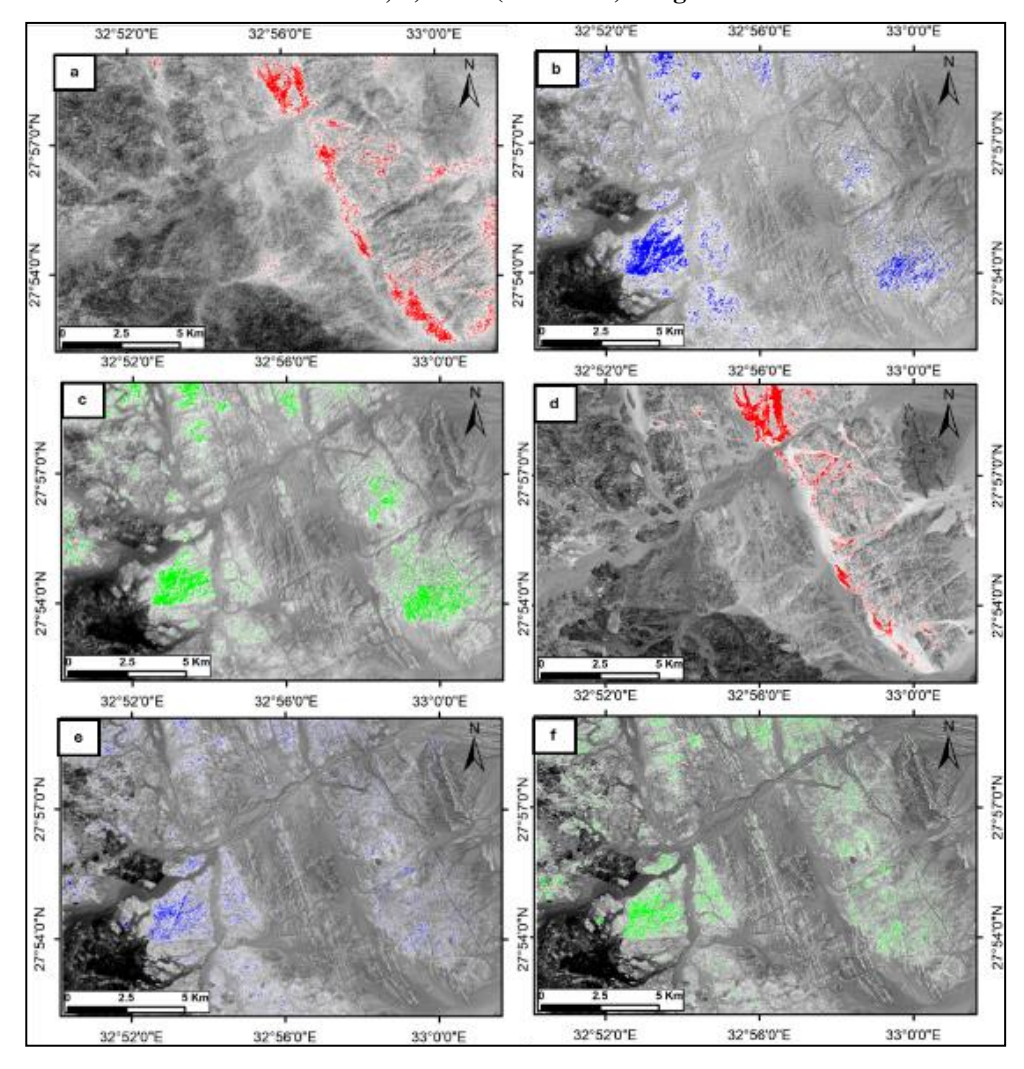


Fig.9. Photographs showing the iron-bearing minerals. a) Ferric iron minerals ASTER 2/1; b) Iron oxides ASTER 4/3; c) 4/2 Gossan ASTER 4/2; d) Ferric iron minerals Sentinel 2B 4/2. e) Iron oxides Sentinel 2B 11/8; f) 4/2 Gossan Sentinel 2B 11/4.

For mapping the hydrothermal alteration zones, the ASTER band ratios (6+9/8), (4/5), (4/6), and (7/6), as well as the Sentinel-2B band ratio (11/12), are used in combination with mineralogical indices (OH/ KI/CI) (Figs. 8c and d).

The ferruginous alteration is recognized using the ASTER for detecting iron minerals (Table 2). Ferric iron concentrate at the outcrops to the east of the study area (Fig. 9a). Iron oxides and gossans occur in the Mus trondjemite and in the A F granite of G. Dara. However, minor iron oxide alteration sites outcrop to the western to northwestern site of the studied succession (Figs. 9 b and c). The use of equivalent band ratios of Sentinel 2B and ASTER for detecting iron-bearing minerals is shown in Table 2. The results are of the same occurrences, but the Sentinel 2B images show high resolution due to the properties of Sentinel 2B MSI (Figs. 9d to f).

Table 2: ASTER and equivalent Sentinel-2 band ratios used for minerals (Kalinowski and Oliver, 2004; in Van der Meer et al., 2014).

Feature	ASTER	Sentinel-2
	Iron	
Ferric Iron, Fe ^{3 +}	2/1	4/3
Ferrous Iron, Fe ²⁺	5/3 + 1/2	12/8 + 3/4
Laterite	4/5	11/12a
Gossan	4/2	11/4
amphibole	5/4	12/1 1
Ferric oxides	4/3	11/8
	Carbonates/Mafic minerals	
Carbonate/Chlorite/Epidote	(7 + 9)/8	-
Epidote/Chlorite/Amphibole	(6+9)/(7+8)	-
Amphibole/MgOH	(6+9)/8	-
Amphibole	6/8	-
Dolomite	(6+8)/7	-
	Silicates	
Sericite/Muscovite/Illite/Smectite	(5+7)/6	-
Alunite, Kaolinite, Pyrophyllite	(4+6)/5	-
Phengitic	5/6	-
Muscovite	7/6	-
Kaolinite	7/5	-
Clay	(5 x 7)/62	-
Alteration	4/5	11/123
Host rock	5/6	-
d ASTE	R bands 5-7 fall within band 12 of Sentine	1-2.

Microscopic Studies

1. Petrography

The gabbro-diorite is composed mainly of plagioclase and pyroxene with minor amounts of hornblende, biotite, and opaque minerals. The plagioclase shows prismatic crystals with lamellar twining that are altered along fractures, while the pyroxene is characterized by high interference colors (Fig. 10a and b). The granodiorite is a medium to coarse-grained rock consisting essentially of plagioclase, orthoclase, and quartz with significant amounts of biotite partly altered to chlorite. Plagioclase is oligoclase in composition and tabular in shape with albite and pericline twinning. Sometimes, it is partly saussuritized. Occasionally, secondary zonation of plagioclase is also recorded. Quartz appears as medium- to coarse-grained anhedral crystals, often filling the intervening gaps among the constituents of the rock, and shows wavy extinction and sometimes cracks (Fig. 10c and d).

The DVs are massive, fine-grained, and black in color. The DVs consist mainly of plagioclase, biotite, and hornblende, partly altered to chlorite and epidote, while the accessory minerals are mainly zircon and iron oxides (Fig. 10e).

The monzogranites are medium to coarse-grained and exhibit color range from white to pink. Petrographically, monzogranite shows hypidiomorphic texture, and it consists of plagioclase, quartz, orthoclase, biotite and minor amphibole. Plagioclase is euhedral to

subhedral crystals varying from 1 mm to 2.3 mm in length and from 0.6 mm to 1mm in width. The plagioclase crystals are often zoned and show lamellar twinning particularly in the unaltered crystals. Sometimes, these crystals are partly or completely altered to sericite. On the other hand, quartz crystals are distinguished by wavy extinction, while orthoclase shows simple twining (Fig. 10 f and g). While the AF granite is medium to coarse-grained, and it shows hypidiomorphic texture with subordinate perthitic textures. It is composed essentially of alkali feldspar (orthoclase or microcline), plagioclase, quartz, muscovite and biotite, with accessory minerals as zircon and sphene. Alkali feldspars are represented by microcline and microcline perthite, while plagioclase is mainly albite in composition represented by subhedral crystals. Quartz occurs as anhedral crystals showing wavy extinction and moderate deformation indicated by fractured borders (Fig. 10h).

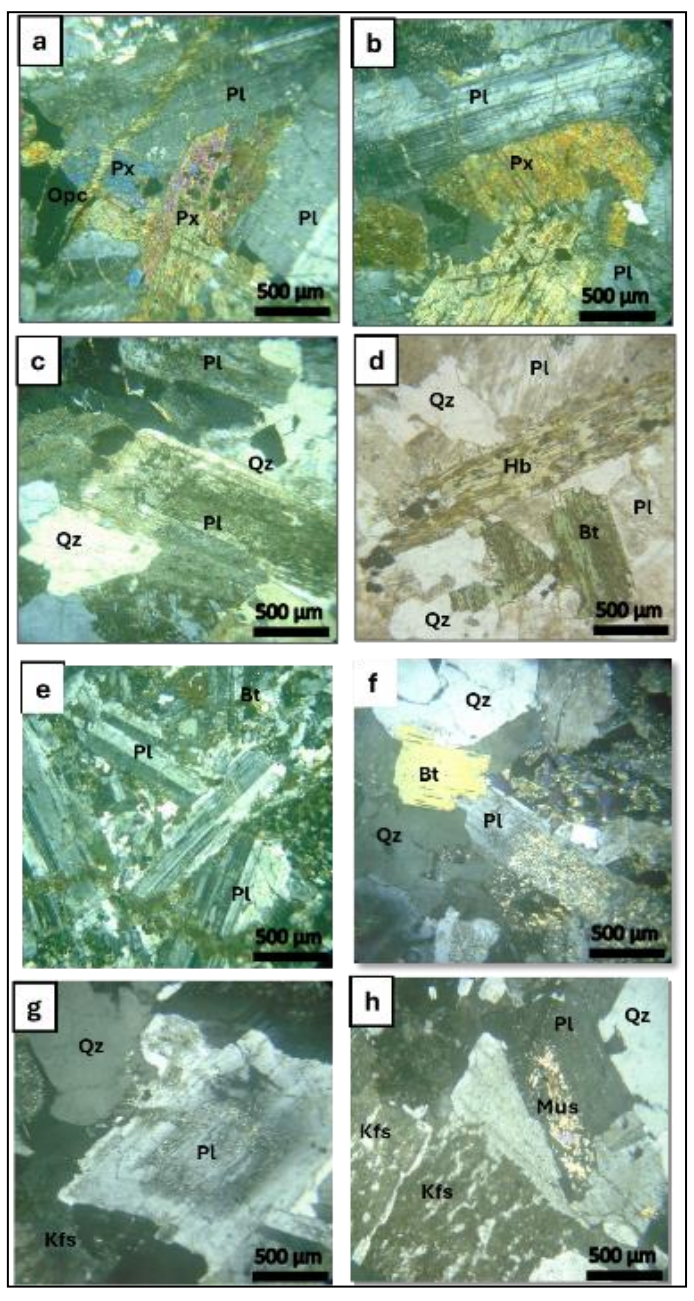


Fig. 10. Photomicrograph of the studied rock units. a) Plagioclase (Pl) crystals fractured and altered with subophitic texture in gabbro-diorite; b) Pyroxene (Px) subhedral crystal with corroded edges in gabbro-diorite; c) Plagioclase (Pl) altered at core and edge in granodiorite; d) Hornblende (Hb) elongated crystal with biotite in granodiorite; e) Plagioclase (Pl) and pyroxene (px) crystals with a fine-grained groundmass in basaltic andesite; f) Plagioclase (Pl) altered partially to sericite at core in monzogranite; g) Plagioclase (Pl) primary zonation with quartz in monzogranite; h) K-Feldspar (Kfs) perthite with quartz (Qz) in AF granite.

2. Ore Minerals

The recorded opaque minerals are mainly sulfides (chalcopyrite, pyrite) with minor galena and sphalerite in addition to supergene minerals as malachite, covellite, and goethite. Chalcopyrite is represented by euhedral to subhedral crystals. In many cases, it is replaced by malachite, sometimes with covellite (Fig. 11a - c). Malachite is characterized by green color, which exists in the host rock and ore microscopic photos. Pyrite occurred as a subhedral crystal (Fig. 11d). Galena and sphalerite occurred as minute crystals (Fig. 11e and f). Other minerals, such as monazite, are recoded as subhedral crystals (Fig. 11g).

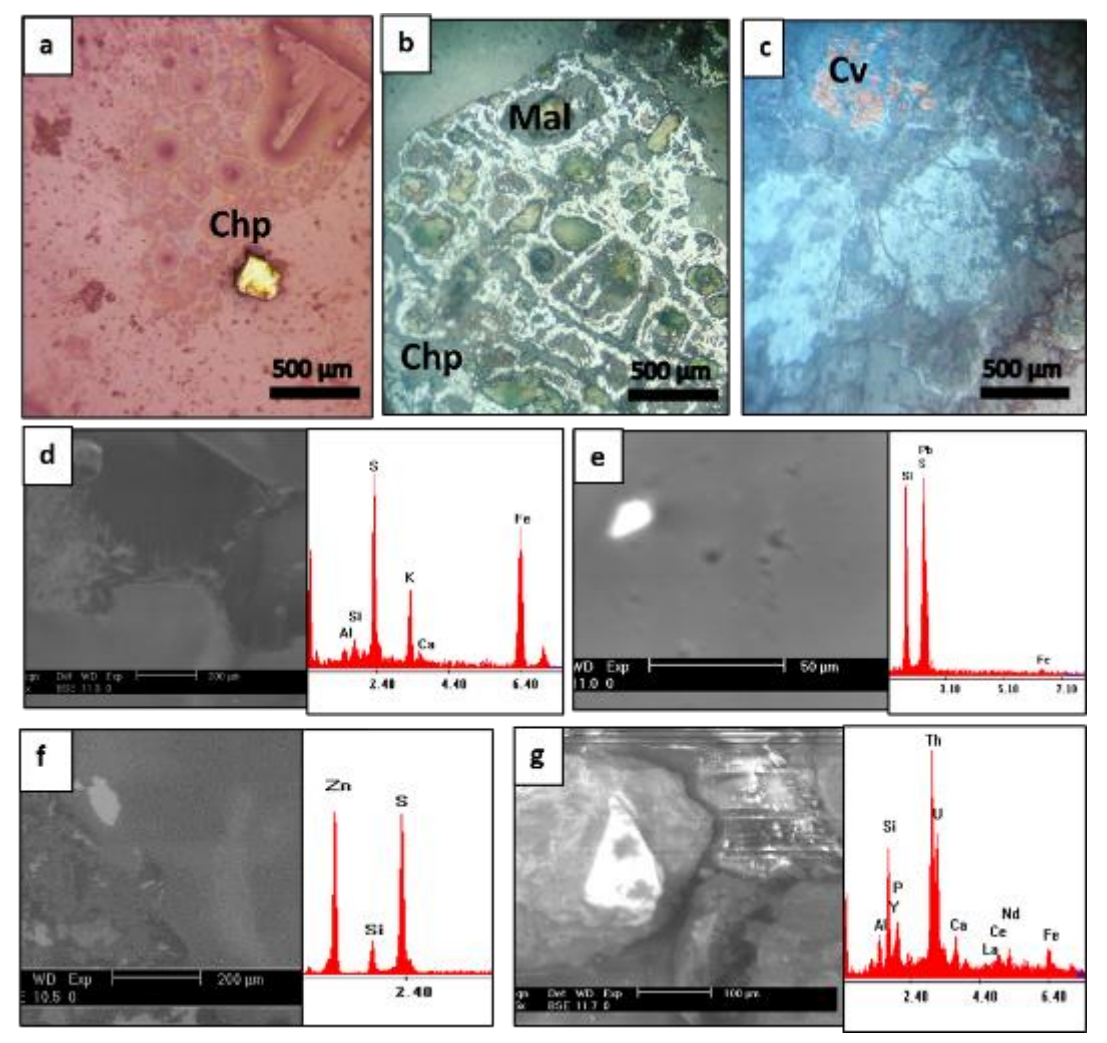


Fig.11. Photomicrographs of ore minerals. a) Chalcopyrite with distinct yellow color; b) malachite after chalcopyrite; c) Covellite; d-g) Scanning Electron microscope of the ore minerals; d) Pyrite; e) Galena; f) Sphalerite; g) Monazite.

Geochemical Investigations

1. Petrochemical Features

Chemical analyses of fifteen representative rock samples (Table 3) are used to distinguish the geochemical characteristics and petrochemical features of the studied rock units. The binary relationships of R1- R2 of De la Roche et al. (1980), silica vs. Na₂O+K₂O of Cox et al. (1979) and Q-P diagram of Debon and Le Fort (1983) exhibit similar behavior, distinguishing these rocks from west to east as: gabbro, gabbro-diorite, granodiorite, tonalite, granite, and AF granites (Figs. 12a-c).

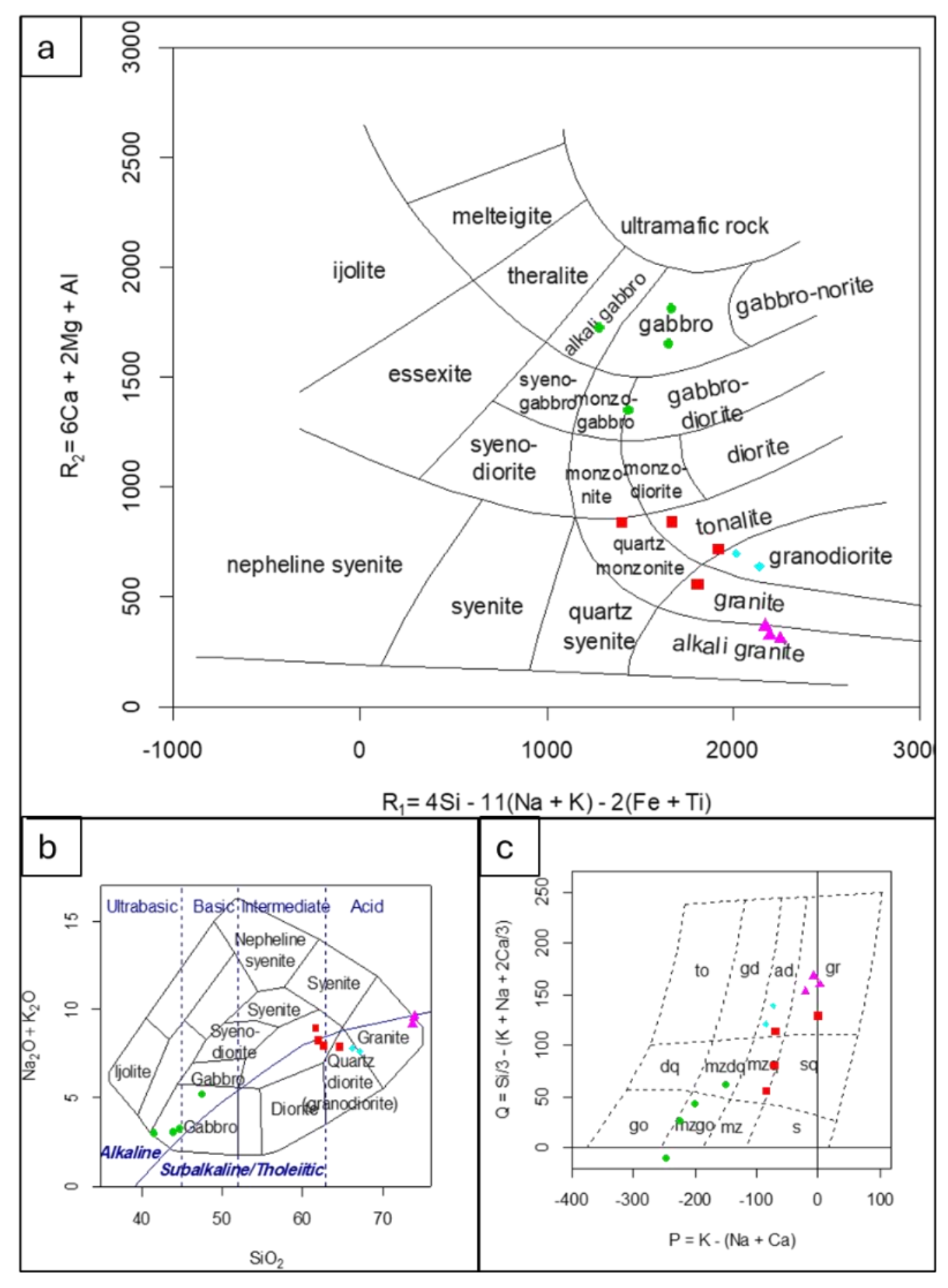


Fig. 12. (a) R1 vs. R2 diagram for the studied rocks of De Laroche et al. (1980); (b) SiO₂ vs. (Na₂O+K₂O) diagram; c) Q-P diagram.

Table 3: Chemical analysis of major and trace elements for the rock units.

Rocks	Gabbro-Diorite					Granodiorite D					Monzogranite		A F granite		
Oxides (%)	4	4.1	4.3	5	1	1.1	3	3.1	7	2.1	8	9	13.1	14	15
SiO,	44.73	41.49	44	47.49	64.63	63.57	62.03	62.66	61.6	53.4	67.13	66.21	73.73	74.01	73.84
TiO,	0.61	1.38	0.58	0.87	0.51	0.4	0.65	0.64	0.65	0.95	0.47	0.54	0.17	0.16	0.19
Al ₂ O ₃	14.05	12.01	13.17	17.45	14.06	17.15	13.85	14.29	14.48	15.69	14.37	14.04	12.81	12.71	12.36
Fe,O,	14.02	16.02	12.86	11.07	4.88	7.93	5.84	7.25	6.02	10.76	4.63	4.81	2.58	1.83	2.23
MnO	0.17	0.16	0.14	0.16	0.08	0.03	0.08	0.04	0.14	0.14	0.13	0.11	0.06	0.07	0.06
MgO	6.53	6.81	7.3	4.47	1.71	0.89	1.76	1.65	1.01	2.45	1.2	1.07	0.17	0.19	0.2
CaO	9.87	7.29	11.13	10.87	3.34	0.3	4.52	1.82	4.71	8.67	2.78	3.43	0.45	0.6	1.07
Na ₂ O	1.74	1.55	1.72	3.06	3.32	0.13	3.09	2.56	3.57	3.03	3.47	3.56	3.64	3.56	3.8
K ₂ O	1.49	1.46	1.36	2.14	4.59	5.79	5.15	5.39	5.41	1.56	4.16	4.27	5.55	6.07	5.72
P,O,	0.3	0.42	0.16	0.24	0.13	0.11	0.19	0.18	0.28	0.35	0.2	0.24	0.03	0.02	0.05
LOI-Flux	4.397	6.877	6.201	1.71	2.819	2.444	2.386	2.577	1.764	2.545	0.992	1.372	0.622	0.597	0.221
						,	Trace Ele	ments (ppi	n)						
Cr	922	1137	933	398	253	310	355	258	10	269	128	96	257	177	255
Co	NA	69	52	NA	76	51	11	26	29	81	56	29	5	NA	NA
Ni	351	545	358	177	NA	36	119	90	8	114	50	20	34	12	39
Cu	16058	36364	8593	198	79	4817	139	6467	138	132	82	120	104	97	70
Zn	175	155	117	59	59	199	80	110	87	125	81	62	68	78	43
Rb	183	203	149	212	208	419	265	241	266	100	205	184	294	287	240
Sr Y	1391	1121 7	1087	1864	518	290	678	393	865	1156	673	717	71	104	234
Zr	26 NA	NA	15 NA	NA NA	201	NA 189	NA 207	271	NA 274	161	16 177	16 133	145	NA 131	NA 119
Nb	8 8	NA NA	NA	21	201	6	25	42	37	9	8	34	26	24	15
Ba	NA	2088	591	NA	258	527	1206	694	1074	1099	1198	244	111	NA	842
Mo	NA	14	22	45	NA	16	NA	4	NA	NA	NA	NA	NA	NA	9
W	116	NA	NA	NA	18	187	NA	NA	36	4	47	NA	57	54	76
Au	NA	1.45	NA	1.5	NA	0.0441	6.13	NA	NA	2.06	0.0225	0.0051	0.0141	0.0027	NA
As	NA	NA	NA	52	NA	36	NA	40	NA	31	NA	13	NA	24	NA
Yb	49	NA	92	143	NA	28	217	51	NA	NA	NA	194	NA	NA	NA
Pb	50	172	122	NA	NA	311	83	NA	86	NA	60	20	57	NA	122
S	365	819	471	228	581	639	516	248	115	184	1118	379	265	122	92
Cl	686	1593	401	763	370	577	542	454	211	687	285	922	199	238	165
	4.00		4.05	2.24	2.11			atios			2.55	2 42		2 12	201
Na K	1.29	1.15	1.27	2.26	2.46	0.1	2.29 4.27	1.89	2.64	2.25	2.57	2.63	2.69	2.63	2.81
K/Na	0.96	1.21	0.89	1.78 0.78	3.81 1.55	4.81	1.87	4.47 2.36	4.49 1.7	1.29 0.58	3.45 1.34	3.54 1.35	4.61 1.71	5.04 1.91	4.75 1.69
K,O/Na,O	0.86	0.94	0.79	0.78	1.38	44.54	1.67	2.11	1.52	0.58	1.2	1.33	1.52	1.71	1.51
Mg	3.94	4.11	4.40	2.70	1.03	0.54	1.06	0.99	0.61	1.48	0.72	0.65	0.10	0.11	0.12
Ca	7.05	5.21	7.95	7.77	2.39	0.34	3.23	1.30	3.37	6.20	1.99	2.45	0.10	0.43	0.76
Rb/Sr	0.13	0.18	0.14	0.11	0.4	1.44	0.39	0.61	0.31	0.20	0.3	0.26	4.14	2.76	1.03
mg#	42.3	40.31	47.31	37.85	32.97	13.17	29.67	24.24	18.8	31.09	26.71	23.79	8.2	12.26	10.77
A/NK	3.14	2.91	3.06	2.37	1.35	2.65	1.3	1.42	1.23	2.35	1.41	1.34	1.07	1.02	0.99
A/CNK	0.63	0.69	0.54	0.64	0.85	2.44	0.73	1.07	0.71	0.7	0.94	0.84	1	0.94	0.86
	1	. 1	•			3.4.0				137 0			α.		

Based on the ratio FeO_t/(FeO_t+MgO) versus SiO₂ and Na₂O+K₂O-CaO vs. SiO₂ diagrams of Frost and Frost (2008), the rocks are ferroan in nature and alkalic-calcic (Fig. 13a and b), while most samples show calk alkaline except gabbro-diorite showing tholeitic nature on the AFM ternary diagram of Irvine and Baragar (1971) (Fig. 13c). Moreover, the plotting on the A/NK-A/CNK binary diagram of Shand (1943) shows that all the samples are metaluminous, except one sample is peraluminous (Fig. 13d).

Using the R1-R2 diagram of Batchelor and Bowden (1985), the samples are plotted in the fields of syn-collisional and late orogenic granites (Fig. 14a). Moreover, according to the geotectonic classification diagram of Pearce et al. (1984). The samples are syn-collision and volcanic arc granites (Fig. 14b). These tectonic settings and the defined alteration types are due to the co-magmatic hydrothermal solutions. On the other hand, using the FeO_t-MgO-Al₂O₃ diagram of Pearce et al. (1977). The gabbro-diorite plots exhibit an ocean island setting (Fig. 14c).

The binary diagrams of Fe_2O_3 vs. MgO, and Fe_2O_3 vs. CaO, given by Hassaan and El-Desoky (2016) and Hassaan et al. (2022) are used for averages of 29 younger granite plutons of the Eastern Desert Central Domain (EDCD) to recognize their geochemical characteristics and distribution. These diagrams separate the three types of granites (monzogranite, syenogranite, and alkali feldspar granites). Plotting of the studied granite samples on Fe_2O_3 vs. MgO, and Fe_2O_3 vs. CaO diagrams (Figs. 15a and 15b) shows that these granites are monzogranite and alkali feldspar granite, in addition to separating the altered samples affected by ferrigination.

The total iron content is high for the gabbro-diorite samples (ranging from 11 to 16 wt%), the granodiorite and monzogranite show values (4-7 wt%), while the A F granite shows low

content of Fe₂O₃ (1–2 wt%). The area is characterized by the formation of iron oxides and gossan zones. The iron oxide minerals are recorded in the field, on polished surfaces, and from remote sensing data. The CaO records high contents in the gabbro-diorite and granodiorite (4.7%), but it shows low content in the A F granite (0.4 wt%). The Na₂O varies from 1.55% in gabbro-diorite to the highest content (3.8%) in the A F granite, while the K_2O shows high values in all granitoids; in the A F granite (6%), while in the other granitoids it ranges from 4.36 to 5.71%. That may be related to the abundance of K-feldspars in the A F granite and mica minerals of other granitoids, in addition to potassic alteration that was recorded in the mineralized granodiorite. Moreover, the K_2O/Na_2O ratio exhibits values more than 1 (1.2 to 2.11) in all granitoids.

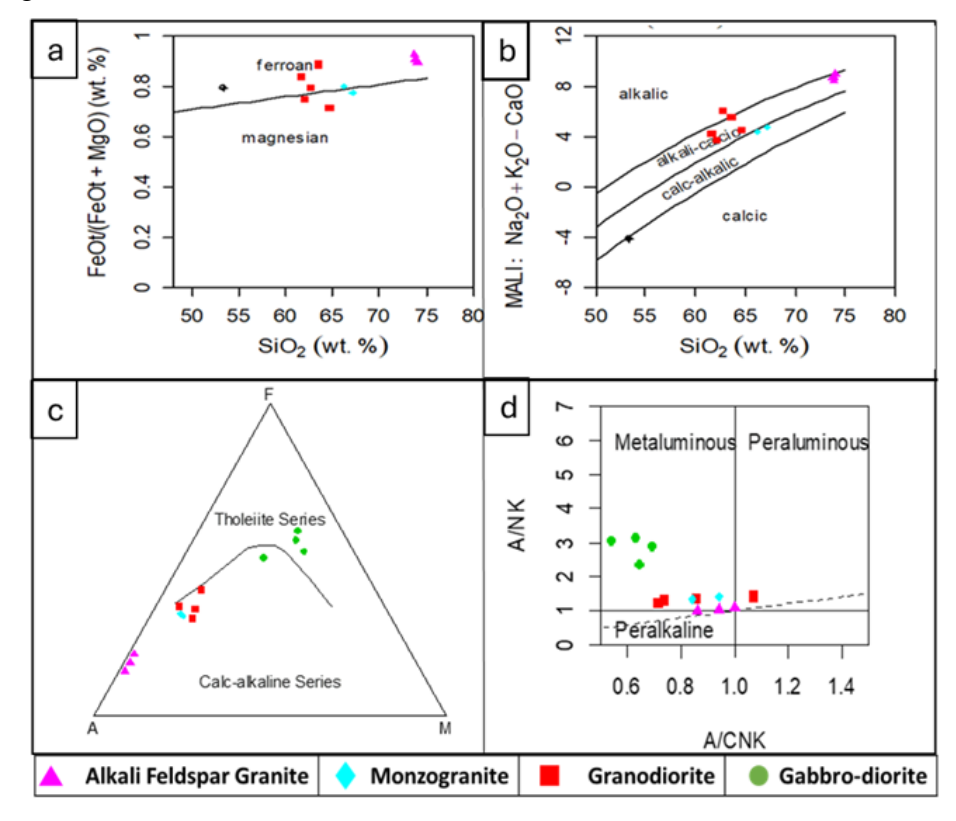


Fig. 13. (a, b) Plots of the studied samples on Frost and Frost (2008) diagrams; c) AFM diagram of Irvine and Baragar (1971); d) A/NK vs. A/CNK diagram of Shand (1943).

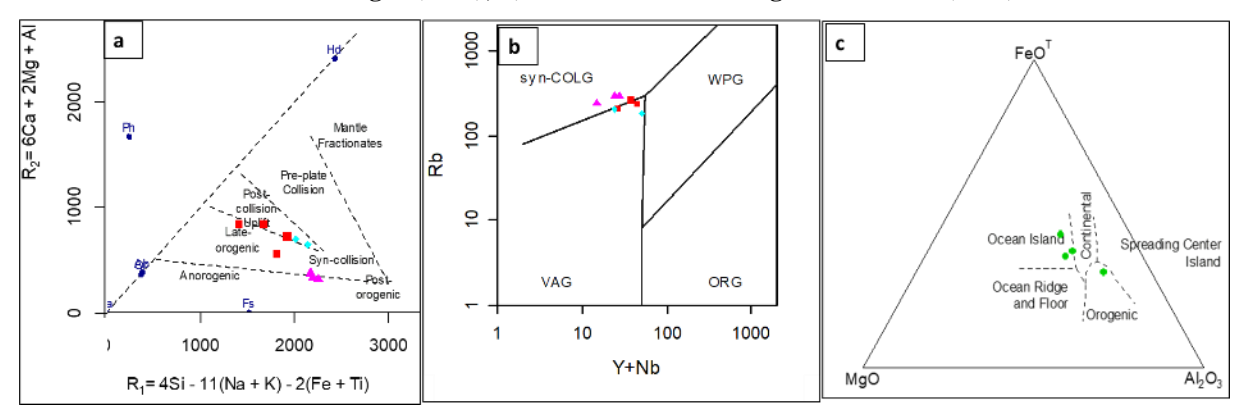


Fig. 14. a) R1-R2 binary diagram of Batchelor and Bowden (1985); (b) Rb vs. Nb+Y binary diagram of Pearce et al. (1984); c) AFM diagram of Pearce et al. (1977).

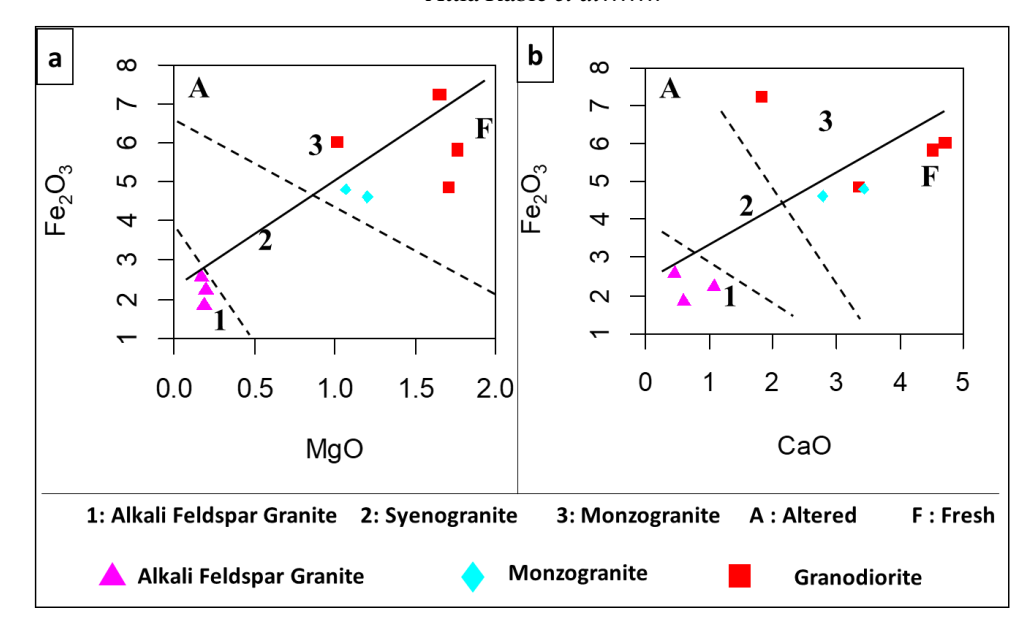


Fig. 15. Plots of binary relationships of (a) Fe₂O₃ vs. CaO; (b) Fe₂O₃ vs. MgO of the studied granites (after Hassaan et al., 2022).

2. Geochemical Characteristics of Trace Elements Distribution

Hassaan et al. (1990, 1991, 2022; 2011) have used the statistical parameters (Clark of concentration, correlation coefficient, and zoning sequence of deposition) to evaluate and reveal the characteristic behavior of trace elements. The parameters are also used to delineate the zone of mineralization.

a) Correlation Relationships

The binary relationships of the analyzed elements vs. Fe_2O_3 and Cu of all samples distinguished the presence of more than one correlation field except Zn and S, pointing to the presence of these metals in more than one phase (e.g., sulfides, oxides, and silicates) (Figs. 16 and 17).

	FeOt	Cr	Co	Ni	Cu	Zn	Rb	Sr	Y	Zr	Nb	Ba	Mo	W	Au	As	Yb	Pb	S	Cl
FeOt	1.00																			
Cr	0.83	1.00																		
Co	0.33	0.14	1.00																	
Ni	0.89	0.97	0.17	1.00																
Cu	0.74	0.85	0.25	0.89	1.00															
Zn	0.67	0.56	0.31	0.52	0.61	1.00														
Rb	-0.42	-0.30	-0.31	-0.39	-0.15	0.17	1.00													
Sr	0.78	0.49	0.11	0.60	0.32	0.20	-0.58	1.00												
Y	0.43	0.44	0.16	0.43	0.32	0.30	-0.55	0.39	1.00											
Zr	-0.63	-0.78	0.12	-0.75	-0.53	-0.21	0.38	-0.59	-0.44	1.00										
Nb	-0.47	-0.59	-0.55	-0.49	-0.41	-0.40	0.22	-0.24	-0.34	0.53	1.00									
Ba	0.30	0.24	0.51	0.38	0.49	0.21	-0.15	0.08	-0.10	0.12	-0.20	1.00								
Mo	0.43	0.50	0.12	0.45	0.14	0.10	-0.25	0.34	0.18	-0.52	-0.35	-0.07	1.00							
W	-0.10	-0.02	-0.21	-0.15	0.00	0.53	0.65	-0.31	0.03	0.02	-0.20	-0.25	-0.18	1.00						
Au	0.13	0.09	-0.03	0.15	0.00	-0.04	-0.07	0.22	-0.26	0.05	0.04	0.39	-0.10	-0.33	1.00					
As	0.10	-0.22	-0.07	-0.18	-0.20	0.14	0.16	0.19	-0.35	0.05	0.26	-0.30	0.00	0.04	-0.01	1.00				
Yb	0.09	0.02	-0.30	0.06	-0.16	-0.18	-0.10	0.32	0.11	-0.14	0.31	-0.16	0.21	-0.33	0.56	0.15	1.00			
Pb	0.22	0.30	0.19	0.24	0.37	0.59	0.57	-0.17	-0.13	-0.08	-0.38	0.36	0.21	0.62	-0.02	-0.12	-0.13	1.00		
\mathbf{S}	0.23	0.28	0.54	0.29	0.37	0.29	0.02	0.06	0.38	-0.09	-0.54	0.44	0.04	0.05	0.08	-0.29	-0.02	0.36	1.00	
Cl	0.71	0.60	0.32	0.70	0.76	0.43	-0.27	0.52	0.25	-0.49	-0.26	0.41	0.01	-0.22	0.25	0.12	0.25	0.19	0.33	1.00

Table 4: Correlation coefficient (r) matrix.

The correlation coefficient (r) matrix (Table 4) shows significant correlated pairs of elements. The Cu shows a strong positive correlation with FeO_t, Cr, Ni, Cl, and Zn, and a medium positive correlation with Ba and Au. Other elements such as Rb, Nb, and Zr show a negative correlation with Cu (Table 4 and Fig. 16). The total iron FeO_t shows very strong to

strong positive correlations with Cr, Ni, Cu, and Sr, and a medium positive correlation with Mo. Other elements, such as Rb and Zr, show a medium negative correlation with the total iron FeOt. The Mo shows medium positive correlation with FeOt, Cr, and Ni, and medium negative correlation with Rb, Nb, and Zr. The W shows positive correlation with Zn, Rb, and Pb. The lead Pb shows medium positive correlations with Zn, Rb, Ba, and W, while showing a negative correlation with Nb.

b) The Clarke of Concentration (CC)

The calculated CC values of the gabbro-diorite samples are shown in Table 5. The reference value is mafic rocks from Turekian and Wedepohl (1961). The gabbro-diorite is distinguished by Au CC values up to 375 and 363, and Cu CC values up to 185 and 418, supporting the presence of Au-Cu deposits. The Mo CC values reach up to 30 in the gabbro-diorite. The lead CC is recorded as 29 in the gabbro-diorite. Other elements are distinguished near normal CC values.

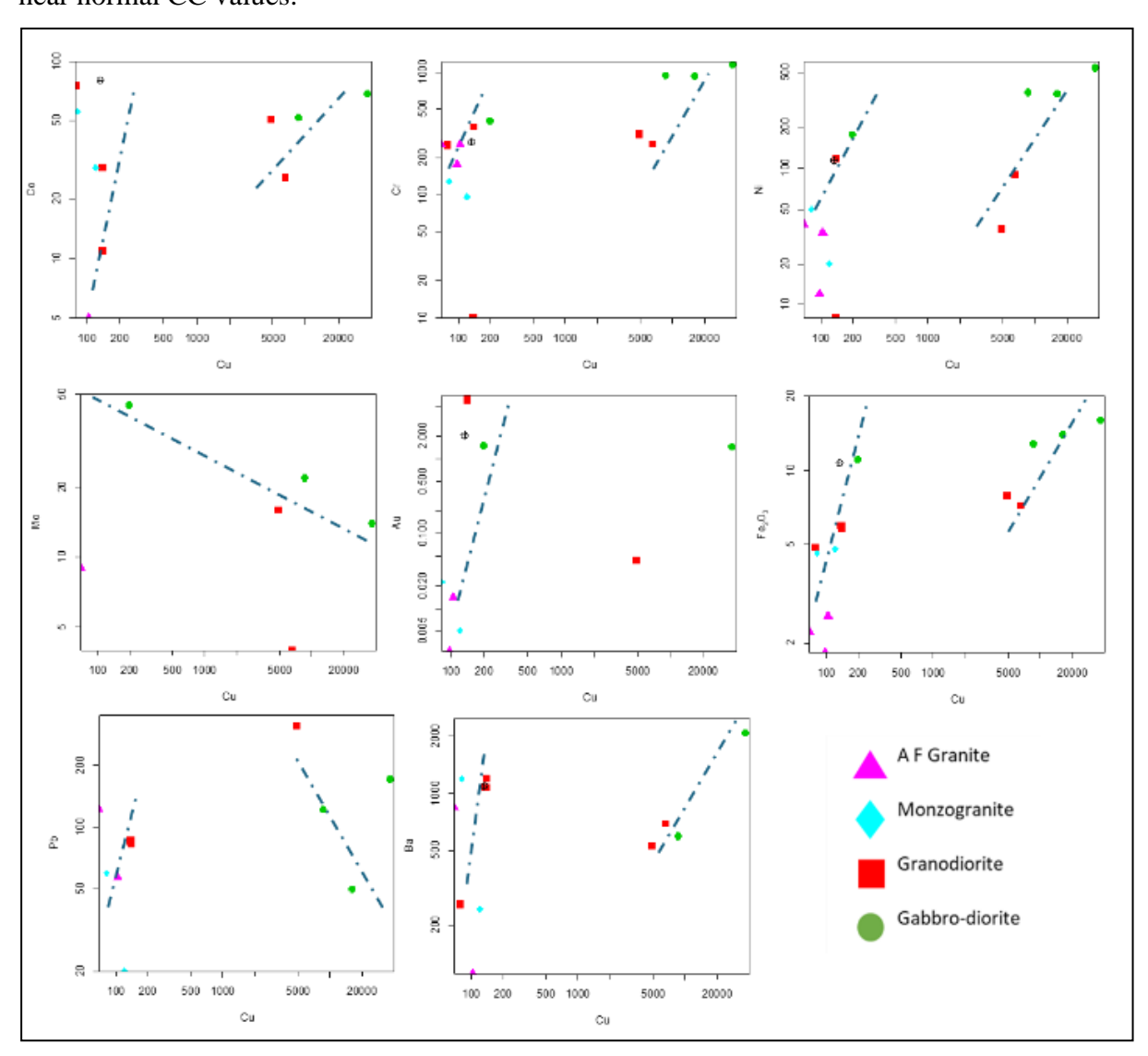


Fig.16. Binary relationships of the Cu vs. trace elements of the analyzed samples.

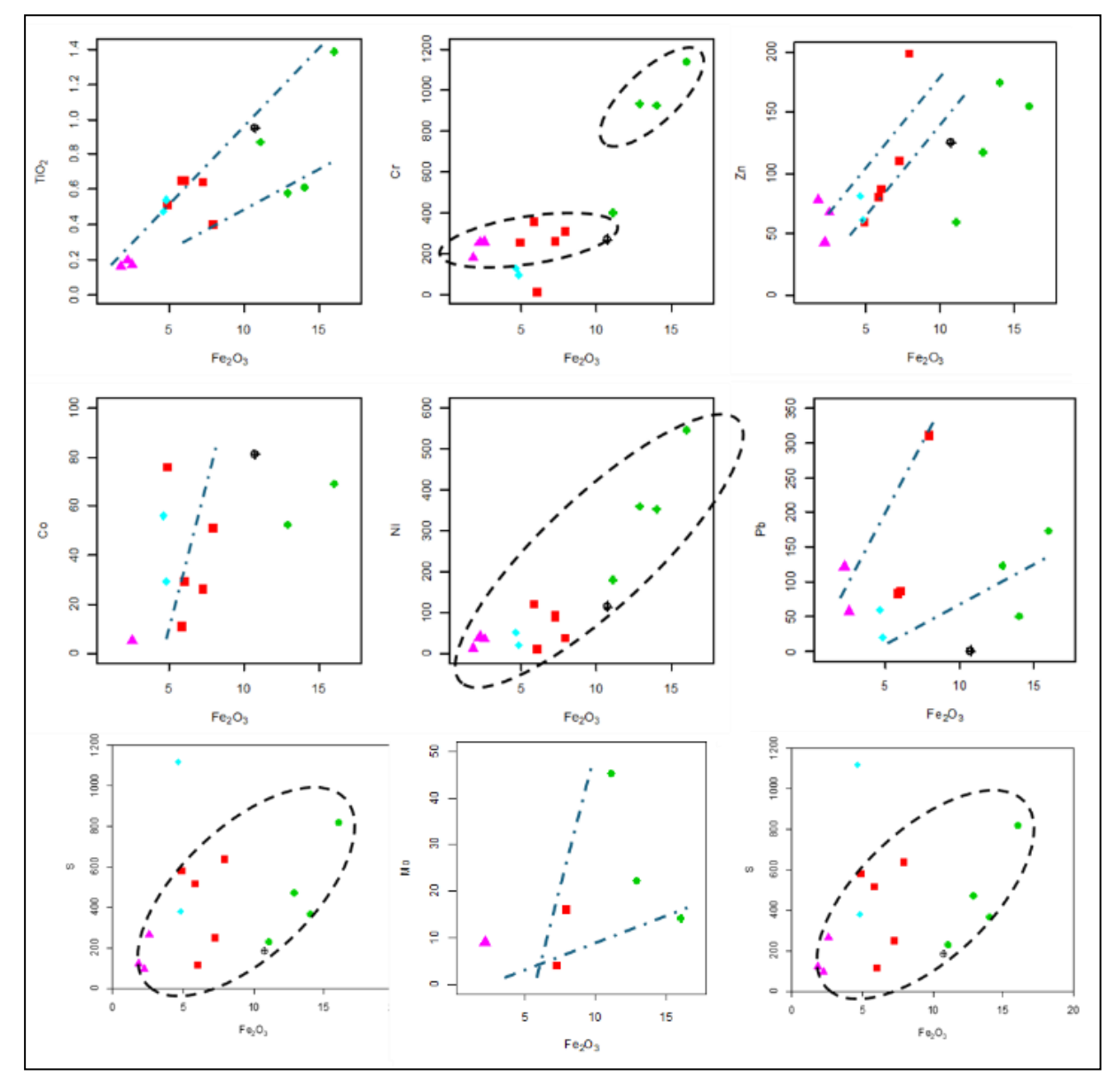


Fig.17. Binary relationships of the Fe₂O₃ vs. trace elements of the analyzed samples.

Table 5: Clark of concentration of the gabbro-diorite samples.

Elamanta	M - 6: -	Gabbro-Diorite								
Elements	Mafic	4	4.1	4.3	5					
Cr	170	5	7	5	2					
Co	48	0	1	1	0					
Ni	130	3	4	3	1					
Cu	87	185	418	99	2					
Zn	105	2	1	1	1					
Ba	330	0	6	2	0					
Mo	1.5	0	9	15	30					
Au	0.004	0	363	0	375					
As	2	0	0	0	26					
Pb	6	8	29	20	0					

The calculated CC values of the granodiorite are shown in Table 6. The reference value is high calcium granite from Turekian and Wedepohl (1961). The granodiorite is distinguished by Au CC values up to 1532 and Cu CC values up to 161 and 216, also supporting the presence of Au-Cu deposits. The Mo CC values reach up to 16 in the granodiorite. The lead CC is recorded as 20, which corresponds with the recorded galena in the granodiorite polished surfaces. The Co values (CC 2–11), Ni values (CC 1-8), and Cr (CC 12-16) show slightly high CC values in most samples.

Elements	High Co.			Granodiorite		
Elements	High Ca -	1.1	1	3	3.1	7
Cr	22	14	12	16	12	0
Co	7	7	11	2	4	4
Ni	15	2	0	8	6	1
Cu	30	161	3	5	216	5
Zn	60	3	1	1	2	1
Ba	420	1	1	3	2	3
Mo	1	16	0	0	4	0
Au	0.004	11	0	1575	0	0
As	1.9	19	0	0	21	0
Pb	15	21	0	6	0	6

Table 6: Clark of concentration of the granodiorite.

The calculated Clark of concentration values for the monzogranite and AF granite samples are shown in Table 7. The reference value is high calcium granite for monzogranite and low calcium granite for AF granite from Turekian and Wedepohl (1961). The granites are distinguished by high Cr CC values up to 63. Moreover, the Ni values show moderate values (3 to 9). The Cu CC values range from 3 to 12, while the Au shows normal CC values (1 to 6).

c) Geochemical Pathfinders

The CC values can be used in the form $\frac{A}{B}$ C (D), where A is the symbol of the main element, B is the main associated element, C is the associated elements, and D is the elements having CC value < 1.

				8		0			
El .		Monzogranite		I C-	AF granite				
Elements	High Ca —	8	9	– Low Ca –	13.1	14	15		
Cr	22	6	4	4.1	63	43	62		
Co	7	8	4	1	5	0	0		
Ni	15	3	1	4.5	8	3	9		
Cu	30	3	4	10	10	10	7		
Zn	60	1	1	39	2	2	1		
Ba	420	3	1	840	0	0	1		
Mo	1	0	0	1.3	0	0	7		
Au	0.004	6	1	0.004	4	1	0		
As	1.9	0	7	1.5	0	16	0		
Pb	15	4	1	19	3	0	6		

Table 7: The Clark of concentration of monzogranite and AF granite

The geochemical spectrum of gabbro-diorite samples recognizes both Au and Cu occupying A, while Pb, Mo are the principal associated elements. The percentage of Au CC represents 46 % and Cu CC 44 % from the summation of CC values of elements, pointing to both elements are the chief ore elements in this rock type. No elements occupy the C, while all the other elements (Ni, Ba, Zn, Co, As) occupy D and exhibit normal dispersed content. The formula of the geochemical spectrum can be expressed as:

$$\frac{Au$$
, $Cu}{Pb, Mo}$ [Ni, Ba, Zn, Co, As].

The geochemical spectrum of granodiorite samples recognizes Au as the chief ore element and Cu as the principal associated element. The recorded elements (Cr, As, Pb, Co) occupying the C sites are the associated elements of the Au-Cu mineral deposit, while the elements (Mo, Ni, Ba, Zn) show normal content. The formula of the geochemical spectrum can be expressed as:

$$\frac{Au}{Cu}$$
 As, Pb, Co, Mo[Ni, Ba, Zn].

For both monzogranite and AF granite, the geochemical spectrum doesn't recognize any chief ore elements; all elements may be associated elements for the Cu-Au mineralization. The arrangement of elements according to the total CC values is as follows: (Cu, Ni, As, Co, Pb, Au, Zn, Mo, Ba).

d) Zoning Coefficient

Zoning coefficient (v) is calculated using CC values of the data. The plotted Clarke of concentration (Cu, Au, Fe, Mo, Zn, Ni, Pb, Co) versus the sites of the studied samples records that the increasing of CC vales from the west to the east for the elements (Cu, Mo, Co) and decreasing for the Au, while other elements (Ni, Co, Fe, Zn) show small decrease (Fig.18). The plotted zoning coefficient (Cu/Au, Fe/Au, Mo/Au, Zn/Au, Ni/Au, Pb/Au, Co/Au) versus the sites in gabbro-diorite and granodiorite in the west of the area records that the sequence of zoning from the bottom upwards is Au, Fe, Zn, Mo, Pb and Cu. (Fig. 19).

Discussion

The study represents the results of the geological-geochemical exploratory works on the Dara area, in which the Cu-Au mineralization in several published studies is recorded (Bishady et al., 2001; Hassaan and Al-Hawary, 1989; Helba et al., 2021b). These studies mentioned the geologic mapping for rock units and their characteristics, their petrographic, petrochemical features age dating of some rock units.

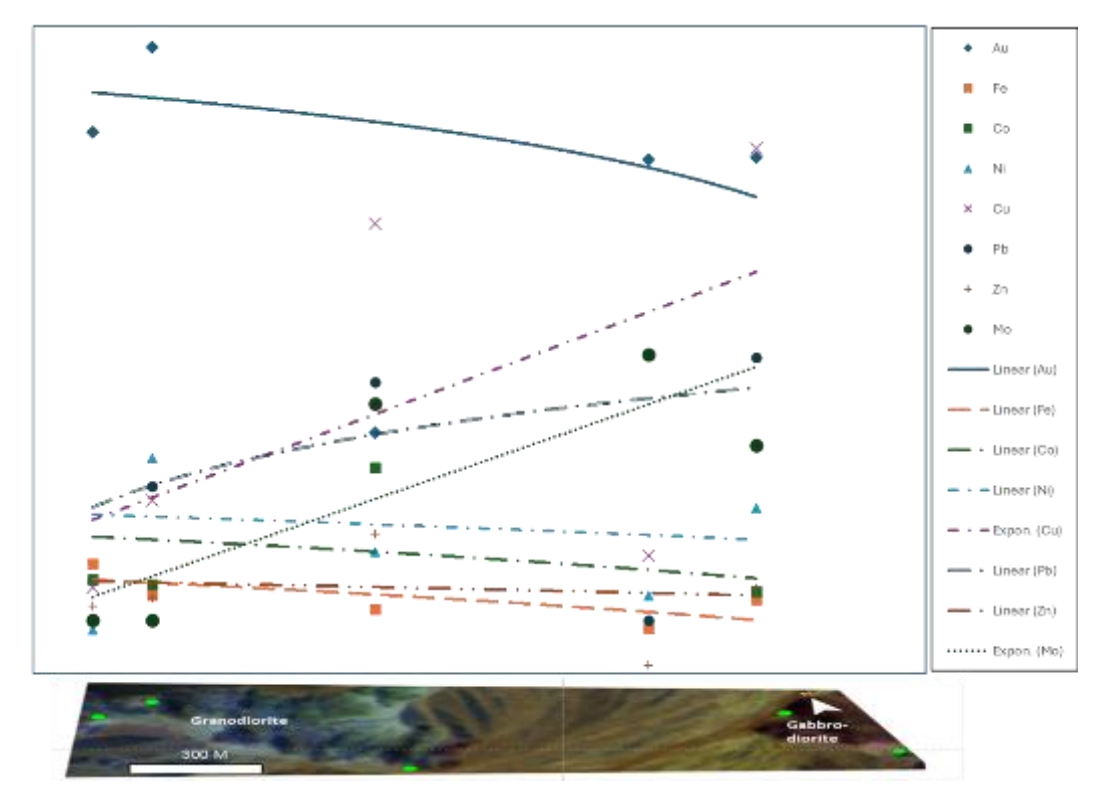


Fig.18. Clarke of concentration distribution.

The field studies, RS processing, petrographic and ore microscopes, chemical analysis of representative rock samples, and lithochemical exploration survey aim to define the mineralized outcrops and geochemical behavior of Au and Cu to evaluate their economic importance using several parameters and factors such as correlation patterns, CC, pathfinder elements, and zoning coefficient. The results of these studies are used to reveal the zonal distribution, explain its setting, and reveal the center of mineralization to be considered as an ore deposit.

The defined rock units are metavolcanics, gabbro-diorites, granodiorites, DVs, monzogranite, and AF granites, which are cut by the post-granitic dykes and quartz veins. Eliwa et al. (2014) documented the development of granite rocks at the NED. The results distinguished four types of granites from older to younger: Mus trondjemite (741 Ma), granodiorites (720 Ma), biotite hornblende granite (BH granite (608–590 Ma), and alkali feldspar granite (AF granite) (600–592 Ma). Accordingly, Mus. trondjemite and granodiorite are attributed to partial melting in the subduction-related regime of the lower oceanic crust, together with a notable

amount of mantle melt. These rocks are genetically unrelated. While the monzogranite (BH granites) may be generated from the lithospheric mantle. Moreover, AF granite magma might have been generated as a result of partial melting of arc ANS crust.

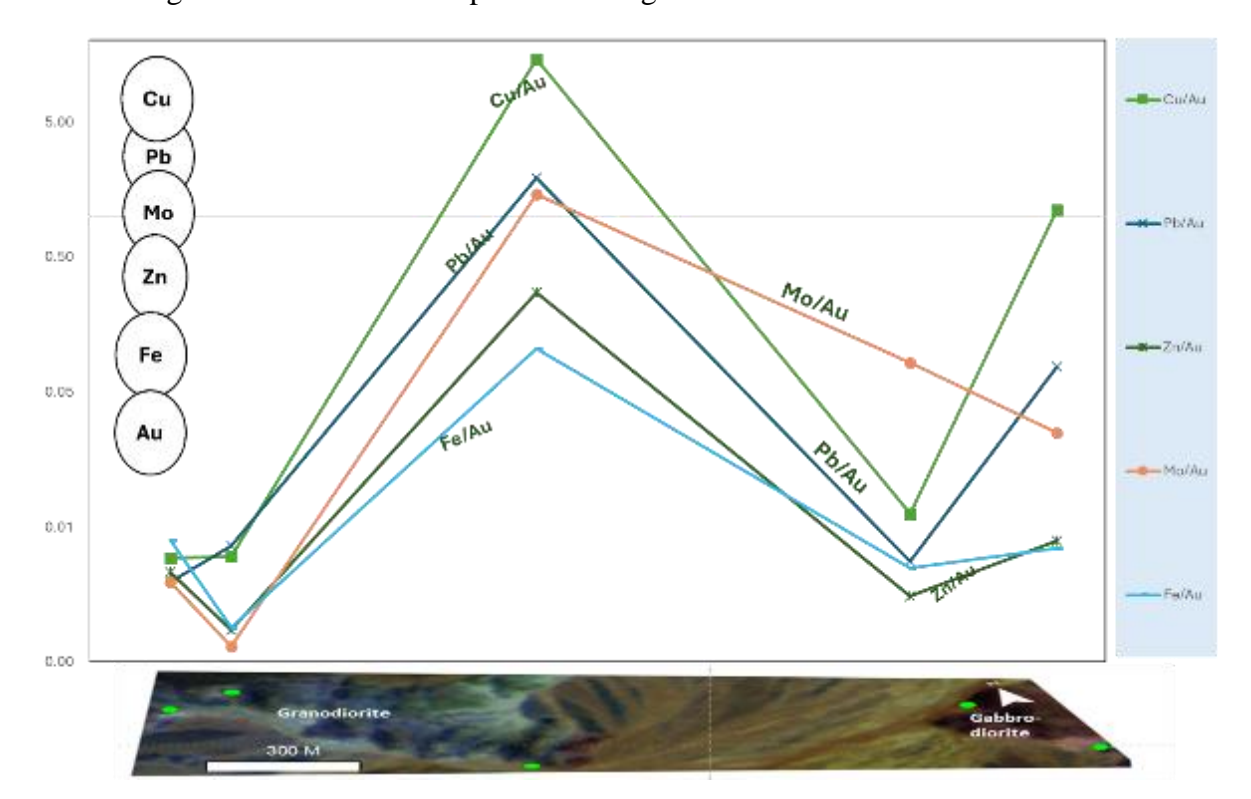


Fig. 19. Zoning coefficient distribution samples.

The RS processing using ASTER and Sentinel 2B distinguished the presence of comagmatic alteration types, viz., propylitic, phyllic, and argillic.

The propylitic: (450° to 600° C) mapped using BR (6+9/8) and Cl index.

The phyllic (200 ° to 450° C) mapped using BR (7/6) and the OH index.

The argillaceous (100° and 300° C) was mapped using the BR (4/6) and KI index. (Figs. 7 and 8). The used BRs and mineral indices define the sites of the alteration types, which are comagmatic and confined to the mineralized gabbro-diorite and granodiorite. The ferruginous alteration is mapped using BR for both the ASTER and Sentinel 2B, which indicated the same sites, but Sentinel 2B is preferred due to the higher resolution.

The geochemical characteristics indicate that gabbro-diorite exhibits metaluminous, tholeiitic characteristics formed in an ocean island setting. While the granodiorite shows metaluminous, ferroan, calc-alkaline nature, formed in a syn-collisional to late orogenic tectonic environment. All the analyzed samples record high content of iron for all samples except AF granite due to the formation of gossan and Fe minerals. The correlation patterns distinguish the presence of more than one correlation field, pointing to the presence of these metals in more than one phase, e.g., sulfides, oxides, and silicates.

The ore microscopic studies define the presence of chalcopyrite, pyrite, galena, iron oxides, and sphalerite. The Au CC values of the gabbro-diorite (CC 363-375) and the granodiorite (CC 11- 1575) while the monzo- and AF granite is low (CC 1- 6). Meanwhile, the Cu CC values for the gabbro-diorite range from (CC 2- 418) and in granodiorite (CC 3 - 216), while in monzo- and AF granites are low (CC 3-10). Other elements show high CC, like Mo and Pb (30 and 21), respectively. The elements exhibit the following spectrum: gabbro-diorite (Au, Cu Pb, Mo, Ni, Ba, Zn, Co, As), granodiorite (Au, Cu, As, Pb, Co, Mo, Ni, Ba, Zn) and monzo- and AF granite (Cu, Ni, As, Co, Pb, Au, Zn, Mo, Ba).

On expressing the CC using the formula $\frac{A}{B}$ C (D), it exhibits that gabbro-diorite, both Au and Cu are the chief ore elements, Pb, and Mo are the main associated elements. In granodiorite, the Au is the chief ore element, and Cu is the main associated element; As, Pb, and Co are associated elements. While in monzo- and AF granite, Cu is the main element. The plotted Clarke of concentration (Cu, Au, Fe, Mo, Zn, Ni, Pb, Co) versus the sites of the studied samples distinguished increasing CC values from the west to the east for the elements (Cu, Mo, Co) and decreasing for the Au while other elements (Ni, Co, Fe, Zn) show lower decrease. The plotted zoning coefficient values versus the sites of the studied samples in gabbro-diorite and granodiorite in the west of the area record that the sequence of zoning from the bottom upwards is Au, Fe, Zn, Mo, Pb, and Cu. The position of the Cu reflects oxidation of its primary sulfide minerals as a weathering product.

Conclusion

The reached conclusions are as follows:

- 1- The rock units at W. Dara are: gabbro-diorites, granodiorites, Dokhan Volcanics, monzogranite, and alkali feldspar granites.
- 2- The remote sensing results show that:
 - a) The obtained lineaments and rose diagram indicate two main trends, NW-SE and NE-SW lineaments.
 - b) The alteration zones, such as argillaceous, phyllic, and propylitic types, point to a hydrothermal co-magmatic origin.
- 3- Petrochemically, the rocks exhibit metaluminous, ferroan, alkali-calcic nature, while gabbro diorite is tholeitic. The rocks were formed in syn-collisional to late orogenic fields, while the gabbro-diorite plots exhibit an ocean island setting.
- 4- The detected ore minerals are sulfides (chalcopyrite, pyrite) with minor galena and sphalerite, with supergene minerals.
- 5- The geochemical spectrum recognizes Au-Cu as the chief ore element for gabbro-diorite, while Au is the chief ore and Cu is the principal associated element for granodiorite.
- 6 The zoning sequence of metals arranged from the bottom upwards is Au, Fe, Mo, Pb and Cu.

Conflict of Interest

The authors declare that there are no conflicts of interest regarding the publication of this manuscript.

References

- Abrams, M.J. and Brown, D., 1984. Silver Bell, Arizona, porphyry copper test site report: Tulsa, Oklahoma. The American Association of Petroleum Geologists, the Joint NASA–Geosat Test Case Project, Final Report, pp. 4–73.
- Abrams, M.J., Brown, D., Lepley, L. and Sadowski, R., 1983. Remote sensing for porphyry copper deposits in southern Arizona. Economic Geology, 78(4), pp. 591–604. https://doi.org/10.2113/GSECONGEO.78.4.591
- Al-Boghdady, B.A.M., Shalaby, M.H., and Bassiouni, M.I., 2003. Copper mineralization of Wadi Dara area, north eastern Desert, Egypt: fluid inclusions and mineral chemistry evidence. In the 5th International Conference on the Geology of the Middle East, pp. 643–658.
- Batchelor, R.A. and Bowden, P., 1985. Petrogenetic interpretation of granitoid rock series using multicationic parameters. Chemical Geology, 48(1–4), pp. 43–55. https://doi.org/10.1016/0009-2541(85)90034-8

- Bentor, Y.K., 1985. The crustal evolution of the Arabo-Nubian Massif with special reference to the Sinai Peninsula. Precambrian Research, 28(1), pp. 1–74. https://doi.org/10.1016/0301-9268(85)90074-9
- Bishady, A.M., Shalaby, M., Eliwa, H.A. and Bassuoni, M.I., 2001. Mineralogical and geochemical studies on the copper mineralized rocks of Wadi Dara area, North Eastern Desert, Egypt. Al-Azhar Bull. of Sci., Proc. of 4th Int. Sci. Conf, pp. 393–430.
- Breitkreuz, C., Eliwa, H., Khalaf, I., Gameel, K.El, Bühler, B., Sergeev, S., Larionov, A. and Murata, M., 2010. Neoproterozoic SHRIMP U-Pb zircon ages of silica-rich Dokhan Volcanics in the North Eastern Desert, Egypt. Precambrian Research, 182(3), pp. 163–174. https://doi.org/10.1016/j.precamres.2010.06.019
- Chavez, P., Berlin, G., and Sowers, L., 1982. Statistical Method for Selecting Landsat MSS Ratios.
- Cox, K.G., Bell, J.D. and Pankhurst, R.J., 1979. The Interpretation of Igneous Rocks. The Interpretation of Igneous Rocks. https://doi.org/10.1007/978-94-017-3373-1
- De la Roche, H., Leterrier, J., Grandclaude, P. and Marchal, M., 1980. A classification of volcanic and plutonic rocks using R1R2-diagram and major-element analyses Its relationships with current nomenclature. Chemical Geology, 29(1–4), pp. 183–210. https://doi.org/10.1016/0009-2541(80)90020-0
- Debon, F. and Le Fort, P., 1983. A chemical–mineralogical classification of common plutonic rocks and associations. Transactions of the Royal Society of Edinburgh: Earth Sciences, 73(3), pp. 135–149. https://doi.org/10.1017/S0263593300010117
- Eliwa, H.A., Breitkreuz, C., Murata, M., Khalaf, I.M., Bühler, B., Itaya, T., Takahashi, T., Hirahara, Y., Miyazaki, T., Kimura, J.I., Shibata, T., Koshi, Y., Kato, Y., Ozawa, H., Daas, M.A., and El Gameel, K., 2014. SIMS zircon U–Pb and mica K–Ar geochronology, and Sr–Nd isotope geochemistry of Neoproterozoic granitoids and their bearing on the evolution of the north eastern Desert, Egypt. Gondwana Research, 25(4), pp. 1570–1598. https://doi.org/10.1016/J.GR.2013.06.006
- Emam, A., Hamimi, Z., El-Fakharani, A., Abdel-Rahman, E., Barreiro, J. G. and Abo-Soliman, M.Y., 2018. Utilization of ASTER and OLI data for lithological mapping of Nugrus-Hafafit area, South Eastern Desert of Egypt. Arabian Journal of Geosciences, 11(23), pp. 1–22. https://doi.org/10.1007/S12517-018-4106-1/FIGURES/14
- Frost, B.R. and Frost, C.D., 2008. A Geochemical Classification for Feldspathic Igneous Rocks. Journal of Petrology, 49(11), pp. 1955–1969. https://doi.org/10.1093/PETROLOGY/EGN054
- Gass, I. and Ed, T.R., 1982. Upper Proterozoic (Pan-African) Calc-Alkaline Magmatism in North-Eastern Africa and Arabia.
- Hassaan, M. and El-Desoky, H., 2016. Granites in the Tectonic Environs of The Nubian Shield, Egypt: Geochemical Characterizations and New Contributions. Current Research in Earth Sciences, 10, pp. 59–103.
- Hassaan, M.M. and Al-Hawary, M.A., 1989. Geochemical exploration in northern Eastern Desert II, mode of occurrence of copper and molybdenum in geochemical dispersion aureoles at Um Balad and Dara. Annals Geol. Surv. Egypt, XVI, pp.159–170.
- Hassaan, M.M., Azzaz, S.A., Soliman, M.M., and El-Badawy, 1991. Use of Some Statistical and Geochemical Parameters in Solving Some Genetic Problems of Sukkari Gold Mineralization, Egypt. 48th I-S.I. Sess., Cairo, pp. 9–17.

- Hassaan, M.M., Omar, S.A., Khalil, A.E., Shahin, T.M., El-Naggar, I.M., Sayyed, M.I., and Hanfi, M.Y., 2022. Prognostic Exploration of U-F-Au-Mo-W Younger Granites for Geochemical Pathfinders, Genetic Affiliations, and Tectonic Setting in El-Erediya-El-Missikat Province, Eastern Desert, Egypt. Minerals 2022, Vol. 12, 12(5), 518. https://doi.org/10.3390/MIN12050518
- Hassaan, M.M., Soliman, M.M., Azzaz, S.A. and Attawiya, M.Y., 1990. Geological Studies on Gold Mineralization at Sukkari, Um Ud and Samut, Eastern Desert, Egypt. Annals of the Geological Survey of Egypt, 16, pp. 89–95.
- Hassaan, M.M., Azzaz, S.A., Soliman, M.M., and El-Badawy, 1991. Use of Some Statistical and Geochemical Parameters in Solving Some Genetic Problems of Sukkari Gold Mineralization, Egypt. 48th I-S.I. Sess., Cairo, pp. 9–17.
- Hassaan, M., 2011. Metallic Ore Deposits of the Nubian Shield in Egypt. Lap Lambert Academic Publ.
- Helba, H.A., Ghonaim, M.A., Khalil, S.O. and El Makky, A.M., 2021. Alteration patterns related to copper mineralization in dioritic rocks at the Dara area, north eastern Desert, Egypt. Arabian Journal of Geosciences, P. 14(12). https://doi.org/10.1007/S12517-021-07495-4
- Huntington, J.F., 1996. The role of remote sensing in finding hydrothermal mineral deposits on earth. CIBA Foundation Symposia, 202, pp. 214–235. https://doi.org/10.1002/9780470514986.ch12
- Inzana, J., Kusky, T., Higgs, G., and Tucker, R., 2003. Supervised classifications of Landsat TM band ratio images and Landsat TM band ratio image with radar for geological interpretations of central Madagascar. Journal of African Earth Sciences, 37(1–2), pp. 59–72. https://doi.org/10.1016/S0899-5362(03)00071-X
- Irvine, T.N. and Baragar, W.R.A., 1971. A Guide to the Chemical Classification of the Common Volcanic Rocks. Canadian Journal of Earth Science, 8, pp. 523-548.
- Jakob, S., Bühler, B., Gloaguen, R., Breitkreuz, C., Eliwa, H.A. and El Gameel, K., 2015. Remote sensing-based improvement of the geological map of the Neoproterozoic Ras Gharib segment in the Eastern Desert (NE-Egypt) using texture features. Journal of African Earth Sciences, 111, pp. 138–147. https://doi.org/10.1016/j.jafrearsci.2015.07.024
- Kviatkovisky, E.M., 1977. Lithochemical methods of prospecting for endogenous ore deposits. Leningrad Nedra.
- Sultan, M., Arvidson, R.E. & Sturchio, N.C., 1986. Mapping of serpentinites in the Eastern Desert of Egypt by using Landsat thematic mapper data, Geology, Geo Science World. Geology, 14.
- Pearce, J. A., Harris, N.B.W., and Tindle, A.G., 1984. Trace Element Discrimination Diagrams for the Tectonic Interpretation of Granitic Rocks. Journal of Petrology, 25(4), pp. 956–983. https://doi.org/10.1093/PETROLOGY/25.4.956
- Pearce, T.H., Gorman, B.E. and Birkett, T.C., 1977. The relationship between major element chemistry and tectonic environment of basic and intermediate volcanic rocks. Earth and Planetary Science Letters, 36(1), pp. 121–132. https://doi.org/10.1016/0012-821X(77)90193-5
- Pieri, D. and Abrams, M., 2004. ASTER watches the world's volcanoes: A new paradigm for volcanological observations from orbit. Journal of Volcanology and Geothermal Research, 135(1), pp. 13–28. https://doi.org/10.1016/j.jvolgeores.2003.12.018

- Pirajno, F., 2009. Hydrothermal Processes and Wall Rock Alteration. Hydrothermal Processes and Mineral Systems, pp. 73–164. https://doi.org/10.1007/978-1-4020-8613-7_2
- Pohl, W.L., 2011. Economic Geology Principles and Practice: Metals, Minerals, Coal, and Hydrocarbons Introduction to Formation and Sustainable Exploitation of Mineral Deposits. In Economic Geology Principles and Practice: Metals, Minerals, Coal and Hydrocarbons Introduction to Formation and Sustainable Exploitation of Mineral Deposits. Wiley-Blackwell. https://doi.org/10.1002/9781444394870
- Pour, A.B. and Hashim, M., 2012. Identifying areas of high economic-potential copper mineralization using ASTER data in the Urumieh-Dokhtar Volcanic Belt, Iran. Advances in Space Research, 49(4), pp. 753–769. https://doi.org/10.1016/j.asr.2011.11.028
- Ridley, J., 2013. Hydrothermal ore deposits I: magmatic and orogenic environments. In Ore Deposit Geology (pp. 92–240). Cambridge University Press. https://doi.org/10.1017/cbo9781139135528.004
- Seedorff, E., Dilles, J.H., Proffett, J.M., Einaudi, M.T., Zurcher, L., Stavast, W.J.A., Johnson, D.A., and Barton, M.D., 2005. Porphyry Deposits: Characteristics and Origin of Hypogene Features. One Hundredth Anniversary Volume. https://doi.org/10.5382/AV100.10
- Shand, S.J., 1943. Eruptive Rocks. Their Genesis, Composition, Classification, and Their Relation to Ore-Deposits with a Chapter on Meteorite. John Wiley and Sons, New York. https://www.scirp.org/reference/referencespapers?referenceid=2953903
- Shebl, A. and Csámer, Á., 2021. Reappraisal of DEMs, Radar, and optical datasets in lineaments extraction with emphasis on the spatial context. Remote Sensing Applications: Society and Environment, 24. https://doi.org/10.1016/J.RSASE.2021.100617
- Spatz, D.M., Wilson, R.T., Pierce, F.W., and Bolm, J.G., 1995. Remote sensing characteristics of porphyry copper systems, western American Cordillera. Arizona Geological Society Digest, 20, pp. 94–108.
- Stern, R.J., and Hedge, C.E., 1985. Geochronologic and isotopic constraints on late Precambrian crustal evolution in the Eastern Desert of Egypt. American Journal of Science, 285(2), pp. 91–127. https://doi.org/10.2475/AJS.285.2.97
- Stern, R.J. and Kröner, A., 1993. Late Precambrian Crustal Evolution in NE Sudan: Isotopic and Geochronologic Constraints. In Source: The Journal of Geology (Vol. 101, Issue 5). http://www.jstor.org/www.jstor.org/stable/
- Stern, R.J., Sellers, G. and Gottfried, D., 1988. Bimodal dike swarms in the North Eastern Desert of Egypt: significance for the origin of late Precambrian A-type granites in Northern Afro-Arabia. The Pan-African Belt of Northeast Africa and Adjacent Areas: Tectonic Evolution and Economic Aspects of a Late Proterozoic Oregon, pp. 147–179.
- Turekian, K.K. and Wedepohl, K.H. 1961. Distribution of the Elements in Some Major Units of the Earth's Crust. GSA Bulletin, Vol. 72, No. 2, pp. 175–192. https://doi.org/10.1130/0016-7606(1961)72[175:DOTEIS]2.0.CO;2
- Willis, K.M., Stern, R.J., and Clauer, N. 1988. Age and geochemistry of late Precambrian sediments of the Hammamat series from the Northeastern desert of Egypt. Precambrian Research, 42(1–2), pp. 173–187. https://doi.org/10.1016/0301-9268(88)90016-2